

Antispasmodic activity of novel 2,4-dichloroanilinium perchlorate hybrid material (I): X-ray crystallography, DFT studies, and molecular docking approach

Emna Jaziri

Université de Carthage

Hitler Louis

University of Calabar

Chaima Gharbi

Université de Carthage

Tomsmith O. Unimuke

University of Calabar

Ernest C. Agwamba

University of Calabar

Gideon E. Mathias

University of Calabar

Wataru Fugita

Tokyo University of Marine Science and Technology

Chérif Ben Nasr

Université de Carthage

Lamia Khedhiri (✉ lkhedhiri.loulou@yahoo.com)

Institut National de Recherche et d'Analyse physico- chimique (INRAP)

Research Article

Keywords: 2,4-dichloroanilinium perchlorate, hybrid materials, spectroscopy, antispasmodic activity, molecular docking

Posted Date: July 6th, 2022

DOI: <https://doi.org/10.21203/rs.3.rs-1754179/v2>

License: © ⓘ This work is licensed under a Creative Commons Attribution 4.0 International License. [Read Full License](#)

Abstract

The intriguing properties of organic-inorganic hybrid materials has resulted in the recent upsurge for more effective hybrid materials with diverse activity, harnessing the advantage of the flexibility and structural diversity imposed by these materials. In line with these, the synthesis, crystallography and structural characterization of a novel perchlorate (2,4-dichloroanilinium perchlorate) organic-inorganic hybrid material is reported. The synthesized structure was characterized by FTIR and NMR techniques. Appropriate computational methods were utilized to correlate the experimentally observed spectroscopic properties as well as other molecular electronic properties. The computational studies were achieved at the DFT/M06-2X/6-311++G(2df,2dp) and aug-cc-pVTZ level of theory. For benchmarking purposes, the PWPB95 functional with D3BJ dispersion correction was utilized. Molecular electronic properties such as the frontier molecular orbitals, Natural bond orbital analysis, Hirshfeld surface analysis, and visual study of weak interaction via non-covalent interaction were considered to understand the molecular diversity of the perchlorate cluster. Hybrid materials often pose diverse bio-activities and as such the anti-spasmodic activity of the studied compound is considered by molecular docking approach.

1. Introduction

The conception for organic-inorganic compounds is an interesting topic in recent years, and attracting much attention of many researchers with innovative applications in industrial, biological and technological areas [1–3]. More recently, organic inorganic frameworks have emerged as an important branch due to their intriguing properties such as photoluminescence and electroluminescence, leading to new functional materials [4–6]. Generally, these materials can combine the prominent characteristics of organic and inorganic parts within a single molecule, showing more advantages, for instance, structural flexibility, thermal stability, chemical resistance, macroscopic shape molding and function versatility [7, 8].

An assortment of strategies has been advanced towards the development of new hybrids materials with oxoanions including perchlorate [9, 10]. In fact, the widespread occurrence of perchlorates has generated considerable interest in diverse fields, particularly, stabilization of PVC, catalysis and pharmacology [11–13]. As a result, perchlorates have been often employed as inorganic building blocks in hybrid compounds with multi-dimensional shapes likely chains, ribbons, layers, or three-dimensional arrangements [14–16]. Benefiting from structural diversities and characteristics of hybrid materials, organic components are an appealing part of hybrid materials, which play important roles in affecting their physical properties.

It has been established that numerous neurological disorders, like spasticity, epilepsy, multiple sclerosis, cerebral palsy, spinal cord injury can be attributed to malfunctioning associated with the GABA_B receptor [17]. Clinically, many chemotherapeutic agents have been used to selectively target GABA_B receptor for the treatment of muscular spasticity associated with CNS disorder. These active agents' binding to the receptor in a large binding extracellular cavity shaped like a Venus flytrap, functions as a disulphide-tethered homodimers receptor [18, 19]. A recent report by Wei [19], shows that Carsonic acid, Diazepam, and Toleterodine have excellent property as muscle relaxant i.e. antispasmodic activities by binding effectively with GluN1/GluN2A NMDA receptor agonist [20], and human neuronal $\alpha 9$ nicotinic acetylcholine receptor (nAChR) [21–26], but unfavourably with the GABA_B receptor.

Several reports on the utilization of molecular docking approach have shown promising discovery in the application of this tool in computer-aided drug design. It has help ease the discovery of the activities of potential chemotherapeutic agent with anti-malaria [23], anthelmintic [24], analeptic [25], anti-ischemic [26], anti-cancer [27], antispasmodic [28], etc. and provided a platform for further clinical investigations. Similarly the application of Density functional theory (DFT) in unrevealing the reactivity, stability, and molecular interactions in both simple and complex systems, has been fully exploited by numerous scientist and has accelerated the discovery of important chemical agent for medicinal purpose [29–31].

In the present investigation, we report the crystal synthesis, structural, spectral, optical, thermal and theoretical calculations such as the frontier molecular orbitals, natural bond orbital analysis, molecular electrostatic potential (MEP), Mulliken atomic charge as well as the Hirshfeld surface analysis and non-covalent interactions of a novel perchlorate crystal of $[C_6H_6Cl_2N]ClO_4$ cluster in conjunction with its potential to act as an inhibitory agent by binding with GABA_B receptor to produce an antispasmodic effect as a muscle relaxant is revealed by molecular docking approach.

2. Methods

2.1 Experimental

2.1.1 Synthesis and crystallization

Compound (**1**) was elaborated as colourless crystals, after a few days, by slow evaporation from an aqueous mixture of 2,4-dichloroaniline (Sigma-Aldrich) and 10% aqueous HClO₄ (70%, Aldrich) solution in a molar ratio of 1:1 at room temperature. The crystals can be stable for months under normal conditions of temperature and humidity

2.1.2. X-ray data collection

Suitable single crystal of (**1**) was selected under a polarizing microscope. The crystallographic data of (**1**) was collected on a Mercury CCD System (Rigaku) at room temperature employing MoK α radiation source ($\lambda = 0.71075 \text{ \AA}$). The intensity data collections were corrected for Lorentz and polarization effects as well as empirical absorption based on multi-scan technique. The structure was solved by direct methods using the SHELX program [32] extended by the Fourier technique and modified following anisotropy. The subsequent successive difference Fourier syntheses generated non-hydrogen atoms. The hydrogen atoms of the ligand were added geometrically and refined using the riding model. The structure was refined with a full-matrix least-squares technique on F^2 with the SHELXL crystallographic software [33] incorporated in the WinGX package [34]. Crystallographic details and processing data of the elaborated compounds are gathered in Table 1. Molecular graphics were performed employing Diamond [35].

Crystallographic data for the structural analysis has been deposited at the Cambridge Crystallographic Data Centre, CCDC No 2151547. These data can be obtained free of charge via <http://www.ccdc.cam.ac.uk/conts/retrieving.html>, or from the CCDC, 12 Union Road, Cambridge, CB2 1EZ, UK; fax: (+ 44) 01223-336-033; e-mail: deposit@ccdc.cam.ac.

2.1.3. Spectroscopic analysis

A Nicolet Impact 410 FT-IR spectrophotometer apparatus was employed to study the infrared spectra of compound (**1**) in the 4000–400 cm^{-1} range. The pellets were prepared by mixing the sample with KBr and compressed into a disk

2.2 Computational methodology

Hirshfeld surface and the associated two-dimensional fingerprint plots were generated through Crystal Explorer software [36] to identify intermolecular interactions within the studied crystals. Quantum chemical calculations were performed from the crystal data with the DFT method at the M06-2X/6-311 ++ G(2df,2pd), and M06-2X/aug-cc-pVTZ level of theory using the Gaussian 16 program [37]. Theoretical calculations were undertaken to assign the NMR resonances to the different crystallographic inequivalent carbon and nitrogen atoms of the unit cell. These calculations were obtained at the M06-2X/6-311 ++ G(2df,2pd), level. The chemical shifts of carbon and nitrogen were calculated on the structure of the organic cation with optimization of protons. For benchmarking and stability assessment of the studied compound, geometry optimization was performed using the M06-2X functional and the more accurate PWPB95 with D3BJ dispersion correction with the split valence 6-311 ++ G(2df,2pd), aug-cc-pVTZ and def2-TZVP basis set. Frequency calculations were in all cases conducted at the same computational level to ascertain the absolute correspondence of the optimized geometry to minimal energy on the potential energy surface. Further appraisal of molecular electronic properties by the frontier molecular orbital

approach, NBO stabilization analysis, and surface topological analysis by non-covalent interaction based on the reduced density gradient module was accomplished with the NBO 7.0, and Multiwfn software [38, 39]. Other molecular visualizations were rendered by the virtual molecular dynamics software (VMD) [40].

2.2.1 Molecular docking procedure

The proteins used for molecular docking were downloaded from the protein data bank and prepared with the biovia discovery studio [41]. The receptors were prepared by defining reactive sites, adding explicit hydrogens and removing water molecules that were not necessary during the docking experiments. The receptor cavity was defined with X, Y, Z coordinates of 26.565395, 28.830558, 192.140465 respectively and size of 20Å, and afterwards converted to pdbqt format with the aid of Autodock 4.0 [42]. The ligand and used for docking experiment was prepared by utilizing the optimized geometry of the studied compound at the M06-2X functional and 6-311 ++ G(2df,2pd) basis set. Then, the respective protein was docked with the studied compound using Autodock vina, and the result output were visualized with PyMol and biovia discovery studio visualizer [40]. The docking investigations and preparation of pdbqt files were accomplished by autodock 4.0 and autodock tools (ADT). It was observed that the scoring function in autoDock is based mainly on the hydrogen bonding, Van der Waals interaction, electrostatic interaction, entropy change upon the binding of the compound to the receptor and solvation. The grid parameter file (GPF) was set 20×20×20Å, 20×20×20, and 20×20×20 along the X, Y, Z coordinate axes.

2.2.2 Docking validation and active site selection

The GABA_B receptor which functions as an obligatory heterodimer of the GBRI and GBR2 subunits and is responsible for the modulatory activity of neurotransmission in the central nervous system was chosen as target for docking experiments. The neuromodulatory activity of the studied compound (**1**) was predicted by passonline (a public repository for bioactivity prediction), therefore the 4MS3 protein of GABA_B receptor was obtained from the protein data bank (www.RSCB.org) based on literature survey. FDA approved neuro-suppressant (benzodiazepam) was as well retrieved from the drug data bank repository and used as standards for comparison. To predict the active site of the receptor, two distinct approaches were employed; first the chosen receptor protein was visualized with the online 3D visualization model in RCSB repository to check the binding conformation and interacting amino acids of the co-crystallized ligand with the receptor protein. Then the pdb files were downloaded and re-docked directly to affirm that the co-crystallized ligand fits back into the active pocket previously visualized. Then to further confirm the active site, the PrankWeb online server (<https://prankweb.cz>) was used to predict the active sites of the chosen pdb file [43]. The predicted active sites based on the z-score was then compared with the amino acid residues in the active site of the co-crystallized receptor complex. The close similarity of the predicted active site and the co-crystallized ligand site was used as the basis for docking the studied compound (**1**) with the chosen 4MS3 proteins.

3. Results And Discussion

3.1 X-ray diffraction study

Parallelepiped shaped transparent crystals of new semiorganic material 2,4-dichloroanilinium perchlorate, (C₆H₆Cl₂N)ClO₄ (**1**) were obtained from an acidic reaction of 2,4-dichloroaniline treated with an equivalent amount of perchloric acid. Crystal data, data collection and refinement of (**1**) are exhibited in Table 1.

Table1: Crystallographic data and structure refinement of [C₆H₆Cl₂N] ClO₄

Chemical formula	$C_6H_6Cl_3NO_4$
Formula weight ($g \cdot mol^{-1}$)	262.48
Temperature (K)	183
Crystal System	Orthorhombic
Space group	<i>Pbca</i>
Unit cell dimensions	$a = 10.4483 (8) \text{ \AA}$ $b = 7.6093 (7) \text{ \AA}$ $c = 23.558 (3) \text{ \AA}$
Z	8
Cell volume (\AA^3)	1873.0 (3)
Absorption coefficient μ (mm^{-1})	0.96
Crystal dimensions (mm^3)	$0.30 \times 0.30 \times 0.30$
Color, shape	colorless, Block
Diffractometer	Mercury CCD System (Rigaku)
q range ($^\circ$)	$q_{\min} = 3.4^\circ, q_{\max} = 27.5^\circ$
Index range (h, k, l)	$h = -13 \rightarrow 13, k = -9 \rightarrow 8, l = -30 \rightarrow 21$
No. of measured, independent and observed with $I > 2\sigma(I)$ reflections	12421, 2125, 1927
R_{int}	0.039
Absorption Correction: Integration	$T_{\min} = 0.611, T_{\max} = 0.749$
Radiation type	Mo (K_α) $\lambda(\text{\AA}) = 0.71075$
R, wR^2	0.054, 0.132
Goodness-of-fit on F^2	1.15
Dr_{\max}, Dr_{\min} ($e \text{ \AA}^{-3}$)	0.44, -0.70

The crystallographic investigation reveals that the asymmetric part of the unit cell contains a 2,4-chloroanilinium cation and a perchlorate anion (Fig. 1). The protonation on the N site of the cation is confirmed from the elongated C-N bond distance [$1.467 (4) \text{ \AA}$] and deprotonation from the anion is confirmed from the Cl-O bond distances and O-Cl-O angles as listed in Table 2.

Table 2
Selected bond lengths and bond angles of (ClO₄)⁻ anion in [C₆H₆Cl₂N]ClO₄.

Bond length (Å)	X-ray	M062X	Bond angles (°)	X-ray	M062X
(ClO₄)⁻ anion					
Cl1—O4	1.422 (2)	1.425	O4—Cl1—O2	110.49 (16)	111.7049
Cl1—O2	1.440 (2)	1.4486	O4—Cl1—O3	111.26 (17)	112.2647
Cl1—O3	1.442 (2)	1.4437	O2—Cl1—O3	109.53 (15)	108.8559
Cl1—O1	1.454 (2)	1.4968	O4—Cl1—O1	109.64 (15)	109.8553
			O2—Cl1—O1	107.98 (16)	106.9794
			O3—Cl1—O1	107.85 (15)	106.9205
RMSD		0.0218			0.8991
[C₆H₆Cl₂N]⁺ cation					
Cl2—C6	1.729 (3)	1.706	C1—C6—C5	119.8 (3)	121.8662
Cl3—C4	1.732 (3)	1.7138	C1—C6—Cl2	121.4 (2)	119.4101
N1—C1	1.467 (4)	1.3118	C5—C6—Cl2	118.8 (2)	118.7237
C2—C1	1.382 (4)	1.361	C2—C1—C6	120.6 (3)	119.5495
C2—C3	1.388 (5)	1.4339	C2—C1—N1	118.2 (3)	119.3973
C6—C1	1.386 (4)	1.4047	C6—C1—N1	121.1 (3)	122.2661
C6—C5	1.392 (4)	1.4007	C2—C3—C4	118.3 (3)	118.3366
C3—C4	1.391 (5)	1.4367	C5—C4—C3	122.1 (3)	120.665
C4—C5	1.378 (4)	1.366	C5—C4—Cl3	118.5 (3)	120.665
			C3—C4—Cl3	119.4 (3)	118.9033
			C4—C5—C6	118.8 (3)	119.1256
			C1—C2—C3	120.3 (3)	120.4567
RMSD		0.0579			1.2667

The atomic arrangement of **(I)** can be divided into an organic and an inorganic parts. The inorganic section is composed of corrugated layers of [ClO₄]⁻ anions and NH₃⁺ groups that extend along the *b*-axis direction, held together by N-H...O hydrogen bonds (Fig. 2). Two such layers cross the unit cell at *z* = (2*n* + 1)/4 (Fig. 3). The residues of the organic groups are located between these layers (Fig. 4, Fig. 5).

Two Cl-O bond distances are shorter [1.422(2) and 1.440(2) Å] and two others are in slightly longer [1.442(2) and 1.454(2) Å]. The elongated Cl-O bond distances is due to the two N-H...O hydrogen bonds between the cation and anion (Table 2). This shows the possible charge transfer between donor N and acceptor O atoms. The O-Cl-O bond angles also vary from a minimum of 107.85(2) to a maximum of 111.26(2), which is deviated from a free ion value of 109.5.

The analysis of the hydrogen bonding network reveals that three O atoms of the perchlorate anion are participated in hydrogen bonds (as acceptors) with the -NH₃⁺ group of the dichloroanilinium cation, forming multiple graph set motifs

(Table 3, Fig. 6). Stabilization in the crystal structure of **(I)** occurs through N-H...O hydrogen bonds, augmented by moderate N-H...Cl (Table 3, Fig. 4), C-H... π interactions (Fig. 7) and electrostatic interactions.

Table 3
Selected hydrogen bonds (\AA , $^\circ$) parameters in $[\text{C}_6\text{H}_6\text{Cl}_2\text{N}]\text{ClO}_4$

$D-H\cdots A$	$D-H$	$H\cdots A$	$D\cdots A$	$D-H\cdots A$
N1-H3...O1 ⁱ	0.89 (5)	2.05 (5)	2.885 (4)	156 (4)
N1-H1...Cl2	0.94 (5)	2.56 (5)	3.054 (3)	113 (3)
N1-H1...O3	0.94 (5)	2.51 (5)	2.854 (4)	102 (3)
N1-H1...O1 ⁱⁱ	0.94 (5)	2.12 (4)	3.000 (4)	155 (4)
N1-H2...O2 ⁱⁱⁱ	0.87 (5)	2.02 (5)	2.892 (4)	176 (5)
N1-H2...O3	0.87 (5)	2.58 (5)	2.854 (4)	99 (4)
Symmetry codes: (i) $x, y+1, z$, (ii) $-x+1, y+1/2, -z+3/2$; (iii) $-x+1/2, y+1/2, z$.				

3.2. Hirshfeld surface analysis

Hirshfeld analysis helps to analyze the molecular contributions towards the packing crystal and as such summarizes information on all intermolecular contacts. This analysis is supported through an enrichment ratio conceding assessing the propensity of elaborated compound to form particular interactions. The topology molecular surfaces in terms of d_{norm} surface (D), shape index (S) and curvedness (C) the title molecules is as shown in Figure 8.

2D Fingerprint plots evincing the occurrence of intermolecular contacts are shown in Fig. 9. Taking into account the 2-D fingerprint plots analysis, the O...H/H...O contributions are prominently evident comprising 43.5% of the overall Hirshfeld surfaces. The enrichment ratio value of 1.76 clearly suggests a fully enriched interaction as being favoured in the crystal assembly, which are portrayed as deep red spots in d_{norm} surface (Fig. 10). The latter contacts, provide evidence for the formation of N-H...O hydrogen bond, are mainly due to the interaction between ClO_4 and $\text{C}_6\text{H}_6\text{Cl}_2\text{N}$ generating ring motifs. Intertwined emerge H...Cl/H...Cl interactions comprising 20.3% of the total Hirshfeld surfaces, indicating the presence of intramolecular N-H...Cl interactions, thus, influencing the molecular conformations. It is clearly visible from the enrichment ratios listed in Table. 4 that these contacts, with $E_{\text{H}\cdots\text{Cl}} = 1.24$ higher than unity, are recognized as being highly favoured. Importantly, intermolecular Cl...O interactions are remarkable contributors into the molecular surface with a percent 13.4% to the Hirshfeld surface. These contacts adopt an enrichment ratio $E_{\text{Cl}\cdots\text{O}} = 1.02$. The solid-state structure exhibit C...H interactions standing at 11.8% to the surface area are characteristic way for C-H... π interactions, which plays a crucial role in building three-dimensional network. Interestingly, this contact is over-represented expressed by $E_{\text{C}\cdots\text{H}} = 1.75$ in the crystal packing, as result of most proportion S_{H} of hydrogen atoms (39.3%) at the molecular surface. The relative contribution in terms of C...Cl interactions (Fig. 5) is reflected 3.2% of the total surface area from C-Cl... π interactions, which are slightly favoured since the $E_{\text{C}\cdots\text{Cl}} = 0.89$ is less than unity. Hydrophobic H...H, O...O and Cl...Cl self-contacts are significantly impoverished, which imply that these last-mentioned possess a repulsive character. The C...O contacts are practically avoided with smaller enrichment ratio $E_{\text{C}\cdots\text{O}} = 0.16$, as they are derived from less important interactions with contributions 0.9% in the Hirshfeld surface. Even though, the remaining rare C...C contacts with 0.6% are recognized as under-represented showing $E_{\text{C}\cdots\text{C}} = 0.82$ lower than unity, indicating the absence of $\pi\cdots\pi$ stacking interactions. It is apparent to note that these contacts have reasonable contribution and are responsible for the formation of three-dimensional networks. From this analysis, we have concluded that O...H and H...Cl followed by C...H contacts have major percentage in the crystal structure.

Table. 4 Contacts, enrichment ratio, chemical proportions on the Hirshfeld surface of $(\text{C}_6\text{H}_6\text{Cl}_2\text{N})\text{ClO}_4$.

	H	O	C	Cl
% Surface	39.3	31.3	8.55	20.85
Enrichment				
H	0.68			
O	1.76	0.24		
C	1.75	0.16	0.82	
Cl	1.24	1.02	0.89	0.55
% Contacts	O...H	H...Cl	O...Cl	C...H
	43.5	20.3	13.4	11.8
	C...Cl	Cl...Cl	O...O	H...H
	3.2	2.4	2.4	1.5
	O...C	C...C		
	0.9	0.6		

3.3 Optimization of the chlorate ion

Prior to synthesis and X-ray crystallographic validation of the obtained crystal structure, the structure as obtained from X-ray crystallography was used for computational studies. The first approach in computational structural analysis is to ensure the stability of the considered molecule and test which computational methodology best describes the crystallographic structure. Based on this notion, several computational methods encompassing the highly parameterized M06-2x functional and the highly accurate PWPB95 with D3BJ dispersion corrected functional which are more reliable methods for predicting the molecular properties of main group organic molecules were utilized in combination with the 6-311++G(2df, 2pd), aug-cc-pVTZ and def2-TZVP basis in gas and solution set to study the various molecular electronic properties of the synthesized compound including its geometrical properties in comparison to the crystallographic data. The obtained bond length and angle for selected bonds and angles is presented in table two alongside the X-ray data, while the detailed computational geometrical properties of the molecule in gas and solution are presented in Table S of supporting information. To accurately and statistically estimate the extent of deviation of the modeled structure from the crystallographic structure, correlational analysis based on the root mean square deviation (RMSD) was used to compare the crystallographic and optimized structure. The obtained results are presented along the bond lengths in Table 2. The computed values of RMSD affirms the absolute concordance of the optimized structure to the experimental structure. The RMSD for the bond lengths of the anionic fragment was calculated to be 0.0218 while the cationic moiety had an RMSD value of 0.0579 for all the functionals, while the RMSD for angle deviation was observed to be 0.8991 Å for the anion and 1.2617 Å for the cationic fragment. The calculated C11-O1, C11-O2, C11-O3, C11-O4 bond lengths for the chlorate fragment were 1.4968, 1.4486, 1.442, and 1.425 Å respectively while the experimental bond lengths were observed to be 1.454, 1.440, 1.442, and 1.422 Å. The calculated C-C bond lengths for the $[C_6H_6Cl_2]^+$ fragment was calculated to be in the range of 1.366 to 1.7138 Å. Specifically, C2-C1, C4-C5 and N1-C1 had the lowest calculated bond length of 1.361, 1.366, and 1.312 Å while the experimental bond lengths were equally observed to be low with values of 1.382, 1.378 and 1.467 Å respectively. The O-C-O bond angles of the anion (ClO₄)⁻ fragment was computed to be in the range of 106.92 to 111.71 Å while the experimental bond angles were observed at 107.85 to 110.49 Å. In the same vein, the C-C-C bond angles of the cation $[C_6H_6Cl_2N]^+$ moiety were computed to be in the range of 118.90 to 121.87 Å while the experimental bond lengths were observed to range from 119.8 to 121.4 Å. The results disclosed both the calculated bond lengths and angle to be in good agreement with the experimental. Thus, the chosen computational methods replicate the crystallographic structure well.

Also, to further appraise the stability of the structure in solution, the geometrical parameters were assessed in gas, polar and non-polar solvents (water and Benzene) to assess the possible changes in properties and behaviour due to solvation. The obtained results as presented in the supporting information file shows that all the computed bond angles and lengths falls in the same range as no dramatic changes were observed in going from gas to solvents thus, prompting considerable stability irrespective of the electronic environment. The calculated RMSD in going from gas to non-polar solvent (benzene) is 0.031 while the calculated RMSD in going from gas to water (polar solvent) was observed to be 0.073 when computed at the M06-2X/6-311 ++ G(d,p) level whereas, the calculated RMSD at the aug-cc-PVTZ was 0.068. therefore, the M06-2x/aug-cc-pVTZ level of theory was selected for further studies based on its ability to reproduce the crystal structure to a higher extent.

3.4 Vibrational Characterization

Molecular vibrational spectroscopy has been successfully utilized in the qualitative and quantitative structural elucidation of several organic and inorganic molecules. The uniqueness of this approach lies in the fact that molecular vibrations are specific to individual molecules and as such the structure-property relationship in molecules can easily be explicated. As a result of the lack of higher symmetry in the considered structure, the vibrational attributes of the compound are well pronounced in both infrared and Raman spectrum. The computational simulations of the vibrational specificities of the studied compound were attained at the M06-2X/6-311 ++ G (2df, 2pd) level of computations. 56 fundamental vibrational moods are noticeable based on the n-6 rule [44–45]. For comparison with the experimental data, statistical analysis based on regression coefficient R² was utilized to effectively assess the level of coherence of the optimized structure with the experimental data. The superposition of the experimental and theoretical vibrational frequencies is presented in Fig. 11. It is evident from literature and several reported data on related structures that theoretical vibrational frequencies are overestimated due to anharmonicity and disparities arising from experimental conditions. Thus, several scaling factors have been proposed to assuage this incongruity, based on this notion, the computed vibrational frequencies were scaled by a factor of 0.967 for better concordance with the experimental values. The FTIR spectrum is segmented into two sections, the first section being the region from 4000 to 2900 cm⁻¹ wavenumbers which is characterized by low and broad intensity bands mainly attributed to the O-H and C-H stretching vibrations, while the second region (dominated by several intense bands) is characterized between 1617 to 1025 cm⁻¹ wavenumbers. The experimental spectrum is characterized by three bands of medium intensity at 3566, 3492 and 3423 cm⁻¹ which corresponds to the NH₂ stretching vibrations. These peaks appear to be broad due to the possible hydration of the NH₂ groups as a result of hydrogen bond formation with the chlorate ion, thus the formation of the third peak at 3423 cm⁻¹ is an affirmation of this reality. OH- groups usually have their characteristic absorbance in this region, the peak at 3423 cm⁻¹ is assigned to the hydrogen bonded O–H band between the anion and cation fragments. The absence of the OH group in the structure indicates that the hydrogen bond between the anion and the cation fragment is strong enough to cause the formation of a pseudo OH absorption peak at this frequency. In the theoretical spectrum these absorptions are quite distinct in gas phase calculations as only two peaks of equal intensity are observed for the NH₂ group, therefore affirming the hydrated nature of the NH₂ group as evident in the experimental spectrum and computational calculations in solution. The absorption bands are calculated at 3526 and 3435 cm⁻¹ wavenumbers respectively. To further confirm this observation, the theoretical spectrum as observed in solution shows an increased intensity for the NH₂ group which could also be attributed to the presence of intermolecular hydrogen bonding. The experimental spectrum also shows two peaks at 3070 and 3172 cm⁻¹ which corresponds to the absorptions of the C-H group. The positions of these peaks are due to the aromatic nature of the CH groups which are sp² hybridized. In the theoretical spectrum, the C-H absorption bands are observed between 3134 to 3140 cm⁻¹. These peaks overlap with the N-H anti-symmetric stretching absorptions at 2937–2785 cm⁻¹ which causes the increased intensity of the peak as observed in the spectrum.

The second region in the FTIR spectrum is characterized by deformation bands and NH bending vibrations. The peak at 1617 cm⁻¹ in the experimental spectrum is assigned to the NH₂ scissoring vibration, this peak overlaps with the C = C band

at 1572 cm^{-1} thus, resulting to the broad nature of the peak. The theoretical spectrum shows this peak at 1708 and 1646 cm^{-1} respectively for the NH_2 scissoring and C = C stretching vibration. The characteristic peak at 1532 cm^{-1} corresponds to the in-plane rocking motion of the NH_2 group which overlaps with the aromatic stretching bands, the calculated absorption is assigned at 1543 cm^{-1} . Other prominent interactions as observed in the experimental spectrum are the bands at 1161, 1116, and 1025 cm^{-1} which correspond to the NH, O-Cl, and CH rocking, stretching and CH rocking deformations respectively. The peak at 1025 cm^{-1} in the experimental spectrum is assigned to the asymmetric O-Cl stretching and twisting deformation. All these vibrations are well reproduced in the computed spectrum, thus indicating the accuracy of the computational method. The overall resistance to changes in dipole moment as a result of NH stretching is an indication of molecular stability, hence the studied structure maintains a stable geometry. To further assess the exact extent of deviation of the computed wavenumbers with the experimental, the correlation analysis based on R^2 values were considered. The result as depicted in Fig. 12 shows an R^2 value of 0.9944 which is very high and therefore affirms the absolute correspondence of the computed wavenumbers to the experimental data, also the scale factor employed greatly reduces the computational incongruity arising from basis set and method of computations.

3.5 Electronic Properties

The understanding of molecular electronic properties of molecules is highly important in computation studies, several approaches exist for the computations of such properties however, the famous Koopman's hypothesis is utilized herein to afford such properties. Molecular descriptors which span through the ionization potential (IP), electron affinity (EA), chemical potential (μ), Chemical hardness (η), and electrophilicity index (ω) are considered. these properties are each unique and tends to unveil a specific electronic property of the studied compound. Table 5 list the various descriptors as computed with the M06-2X/6-311++G(2df,2pd and aug-cc-pVTZ basis set. in line with the notion of Koopmans' ionization potential and electron affinity are absolute values of the negative of HOMO and LUMO respectively [46] thus, the ease of electron acceptance or donation is very much dependent on these two parameters and higher or lower tendencies of charge transfer is also appraised by increased or decreased values of IP and EA respectively [31]. The inference from the results in table is that the compound possesses high probability for electron acceptance and a considerable aptitude for electron donation, this assertion is affirmed by the high IP value and low EA value which are computed to be 9.3515 eV and 1.5532 eV respectively. Molecules with high HOMO or IP values are generally less stable compared to species with low HOMO values due to the less amount of energy required for electronic transitions thus, the studied compound is more prone to accept charge density than donate. The energy gap is conceivably the most significant of these molecular descriptors, reasons that it holistically explicates molecular stability and kinetic reactivity by mere considerations of the difference in quantized quantum states peculiar to electronic transitions from the HOMO to the LUMO and vice versa. Thus, molecular species are considered stable if the energy gap is high enough, such that electronic transition from HOMO to LUMO is not easily assessable, and on the other hand, species are considered reactive if these transitions are highly feasible with less amount of energy. Based on these concepts, the studied compound could be regarded as being considerably stable due to its energy gap which is computed to be 7.7983 eV. This value is comparable with the energy gap suggested for conductors and insulator materials which should be above 5.56 eV [47–48]. However, due to the paramagnetic nature of the studied compound due to unpaired electrons, the most feasible transitions within the studied compound results form the singlet occupied molecular orbital and the singlet unoccupied molecular orbital thus confirming its high potential to accept electrons as revealed by the IP value. Therefore, the compound could be termed as species with less propensity to exchange electron density with eminent environment and could display high tendencies of reactivity towards hard bases. The influence of solvation on these molecular properties was also considered and the results likewise discloses that solvent polarity affected the electronic properties to a minimal extent as only slight changes in energy gap is observed to occur. The exact increase in energy gap due to solvation is observed to be 1.05% and 0.64% in water and benzene respectively. The localization of frontier molecular orbitals were also determined for the $(\text{C}_6\text{H}_6\text{Cl}_2\text{N})\text{ClO}_4$ structure (Fig. 13a). it is apparent that, the HOMO is located on the lone pairs of Cl atoms in the cation, while the LUMO is localized over the entire aromatic ring and the NH group. The proximate localization of these molecular orbitals is directly related to

the nature of the feasible inter- and intra-molecular interactions within the perchlorate cluster and thus, aid the quantization of orbital density leading to the understanding of the energetics of the studied system. The energy distribution is depicted in **Fig. 13b**.

Table 5
Calculated quantum descriptors of $(C_6H_6Cl_2N)ClO_4$

	EG	IP	EA	$-\mu$	χ	η	ω
M06-2X/6-311 ++ G(2df,2pd)							
Gas	7.7983	9.3515	1.5532	-5.4524	5.4524	3.8991	3.8122
Water	8.8445	9.7477	0.9032	-5.3254	5.3254	4.4223	3.2065
Benzène	8.4396	9.6829	1.2433	-5.4631	5.4631	4.2198	3.5364
M06-2X/aug-cc-pVTZ							
Gas	7.8301	9.3858	1.5557	-5.4707	5.4707	3.9154	3.8219
Water	8.8565	9.7490	0.8925	-5.3208	5.3208	4.4283	3.1966
Benzène	8.4875	9.7278	1.2403	-5.4841	5.4841	4.2438	3.5434

3.6 Natural Bond Orbitals Analysis and Charge Delocalization

Molecular stabilization catalysed by charge density transfer or the delocalization of electrons can be described by considering the second order perturbation theory analysis of the Lewis and non-Lewis's donor and acceptor interactions existing within the $(C_6H_6Cl_2N)ClO_4$ molecule in different solvents respectively. Such interactions do not only show the preferred stabilization mechanism but also elucidates the exact interactions of each set of molecular charge transfer or excitations within each quantum state of the investigated molecule. Charge transfer or delocalization of electrons within molecular systems is affected by differences in the electronic medium for which the compound exists and as such plays a role in the stability of the investigated molecule [19]. The second order perturbation energy of the investigated complex is presented in Table 6. The most important contributions to molecular stability are the interactions resulting from the delocalization of electrons density from the perchlorate (ClO_4) anion to the benzene ring. These interactions are prompted by charge transfer from oxygen lone pairs of the ClO_4 fragment to the sigma antibonding orbitals of nitrogen and hydrogen atoms of the cationic moiety ($C_6H_6Cl_2N$) and account for a greater stabilization enthalpy in the range of 11.39 kcal/mol to 30.25 kcal/mol in gas phase. This interactions resulted from $LP(3)O16 \rightarrow \sigma^*(N12-H14)$, $LP(3)Cl11 \rightarrow LP^*(1)C6$ and $\sigma^*C3-C4 \rightarrow \sigma^*C1-C2$ with stabilization enthalpies of 23.87 kcal/mol, 30.25 kcal/mol, and 31.91 kcal/mol respectively. The influence of solvation on the observed stabilization enthalpy was carefully observed so as to further appraise the differences in molecular behaviour and stability in polar and non-polar solvents. The results of the stabilization energies in different solvents reveals substantial differences in the E2 energy. The total calculated stabilization energies in gas phase are quite higher than the computed energies in solvent phases, the total charge density delocalization between the lone pairs and pi-antibonding orbitals is calculated to 43.13 kcal/mol in gas phase and this is observed to slightly decrease by 0.06% in water and 0.34 % n benzene. The total change in electron transfer ($\Delta E_{LP-\sigma^*}$) was also, observed to be favoured for the lone pair excitation to sigma bonds than the pi-bonds. The total $\Delta E_{LP-\sigma^*}$ charge density delocalization from lone pairs to sigma bonds was calculated to 83.07 kcal/mol in gas phase which is the highest intermolecular stabilization interactions observed. These results suggest that the studied compound is mostly stabilized by charge transfer delocalization via pi back-donation from the ClO_4 anionic group to the aromatic ring. $LP \rightarrow \sigma^*$ delocalization of electron density is also observed to be the most dominant interaction observed and plays the major role in stabilizing the molecule than $\pi \rightarrow \pi^*$, and $\sigma \rightarrow \sigma^*$ charge transfer in both gas and solution.

Table 6
Resulting Energies of Donor-Acceptor Interactions as revealed by the Natural Bond Orbital Analysis in gas and solvent phases

Gas					Water			Benzène		
Donor (i)	Acceptor (j)	E(2)a [kcal/mol]	E (j) – E(i)b [a.u.]	F (i,j)c [a.u.]	E(2)a [kcal/mol]	E (j) – E(i)b [a.u.]	F (i,j)c [a.u.]	E(2)a [kcal/mol]	E (j) – E(i)b [a.u.]	F (i,j)c [a.u.]
LP*(1)C6	π^* C1-C2	11.39	0.21	0.098	11.57	0.20	0.100	11.35	0.21	0.099
	π^* C4-C5	18.08	0.17	0.105	17.42	0.17	0.105	17.69	0.17	0.013
LP(3)Cl10	π^* C4-C5	13.66	0.43	0.097	14.08	0.42	0.098	13.75	0.43	0.097
Δ ETLP- π^*		43.13			43.07			42.79		
LP(2)O17	σ^* Cl15-O18	10.26	0.66	0.104	7.50	0.66	0.090	7.50	0.68	0.091
	σ^* Cl15-O19	10.80	0.65	0.107	10.48	0.65	0.106	10.70	0.65	0.107
LP(2)O18	σ^* Cl15-O19	12.06	0.65	0.114	11.94	0.66	0.114	12.47	0.66	0.116
LP(2)O19	σ^* ClO17	11.62	0.66	0.112	9.22	0.66	0.100	10.18	0.66	0.105
LP(3)O17	σ^* Cl15-O16	14.46	0.58	0.117	11.97	0.63	0.111	12.25	0.61	0.111
LP(3)O16	σ^* N12-H14	23.87	0.82	0.180	5.58	0.87	0.090	12.81	0.85	0.135
Δ ETLP- σ^*		83.07			56.69			65.91		
LP(3)Cl11	LP*(1)C6	30.25	0.24	0.124	32.91	0.24	0.127	31.81	0.24	0.126
π^* C3-N12	π^* C4-C5	6.75	0.05	0.08	28.39	0.02	0.081	41.55	0.01	0.81
π C1-C2	LP*(1)	43.08	0.18	0.126	34.96	0.20	0.118	38.92	0.19	1.122

3.7. Molecular Electrostatic Potential analysis

The visualization of molecular electrostatic potential surfaces is highly essential for the wholistic comprehension of bio-interaction, hydrogen bonding interactions as well as the detection of potential reactive sites in molecules. Regions of high electron densities are explicated by low values of electrostatic potential and high ESP values often expresses the relative absence of electron density [42]. To understand and predict the most susceptible regions of both nucleophilic and electrophilic reactions, the ESP isosurface plot is obtained from the M06-2X/6-311++g(2df,2pd) optimized geometry. The MEP isosurface is presented in Fig. 14. It clearly shows that the negative areas are located on oxygen atoms of the perchlorate anion and on the aromatic ring, while the positive zone is located on the hydrogen bonded to nitrogen, in accordance with the Mulliken charges (Table 7). Regions of low electrostatic potential density are designated in blue while the red shows negative ESP regions respectively. The ESP isosurface clearly shows that regions of high electron density which could act as nucleophilic sites are localized on the oxygen atoms of the perchlorate anion whereas, the region with the strongest attraction potential is the red-coloured surface on the aromatic ring and thus, high propensity for electrophilic attack. Positive ESP regions are clearly explicated on the hydrogen atoms of the NH group as clearly revealed in white color.

3.8. Mulliken population analysis

The atomic charge was employed to elucidate the processes of charge transfer in chemical reactions. The Mulliken charge distribution of all atoms is given in Table 7. The atoms of the organic molecule are numbered as follows (Fig. 15):

The atomic charge distribution shows that, for the $[\text{ClO}_4]^-$ anion, the Cl ion have positive charge, the most negative atoms being the oxygen (Table 7), in agreement with the previous MEP results (Fig. 14). For the organic entity, the nitrogen atom is negatively charged, while carbon atoms C1, C2 and C5 have positive charges. The C3, C4 and C6 have negative charges, while the Cl7 and Cl9 are positively charged. All hydrogen atoms carry positive charge (Table 7). These results show an electronic charge transfer of 0.13 e from the anion to the cation.

Table 7
Mulliken charge distribution in the organic cations of
 $(\text{C}_6\text{H}_6\text{Cl}_2\text{N})\text{ClO}_4$

Atom	Charge distribution
Cl	1.477516
O	-0.543718 ; -0.701627 ; -0.557709 ; -0.550857
C1	0.078734
C2	1.037627
C3	-0.658953
H(C3)	0.198147
C4	-0.475237
H(C4)	0.222445
C5	0.279696
C6	-0.808516
H(C6)	0.241466
Cl7	0.226077
N8	-1.275117
H(N8)	0.495817 ; 0.598678 ; 0.484233
Cl9	0.231298
Cation charge	0.87
Anion charge	-0.87

3.9 Visual study of weak interactions

Non-covalent interactions based on the reduced density gradient (RDG) is perhaps one of the most frequently utilized method to study weak interactions especially interactions occurring in low density regions [49] non-covalent interaction offers profound information regarding diverse condensed phase behaviour of molecules as well as their special orientation in biological systems. The exact type of intermolecular interaction existing within molecules could be accounted for by analysing their eigenvalue sign which exemplifies density fluctuations and distinguishes stabilizing and non-stabilizing interactions. However, if the eigenfunction (sign $(\lambda_2) \rho$ is less than zero $\lambda_2 < 0$, such interaction is described as non-covalent interaction, similar implication is applicable for eigenfunction (sign $(\lambda_2) \rho$ greater than zero $\lambda_2 > 0$, which primed such interaction to be repulsive in nature. The non-covalent interaction plot for the studied compound is presented in Fig. 16 along with the colour code. it is apparent from the figure that Van der Waals and steric repulsive interaction constitute the

predominant forces of intermolecular interactions within the studied compound. The blue colour signifies hydrogen bond, whereas the green and red denotes Van Der Waals and steric cyclic effect respectively. The crystal structure also indicates the presence of hydrogen bond between N-H...O and N-H...Cl. The sign of their eigenvalues ($\lambda_2^* \rho$) ranges from -0.020 to -0.010 Å in the fingerprint plot indicating significant steric contributions from the aromatic ring to molecular stability. The brightly intense green colour in the RDG isosurface confirms the presence of strong VDW interactions and suggest the compound to be stabilized by these forces of interaction.

3.10 Molecular docking

Molecular docking approach has evolved as an essential computational approach to quickly assess molecular interactions between compounds and biological enzymes, as well as predict possible binding mechanisms in biological process [23, 24]. This approach has been utilized herein to evaluate the bio-activity profile of the studied perchlorate ion cluster. The autodock vina tools and corresponding visualizers were deployed for this purpose. Figure 17 depicts the 3D and 2D interactions of the studied compound with the chosen receptor proteins in comparison with a conventional antispasmodic agent (benzodiazepine) From **Fig. 17 (a-b)**, the interaction of (1) with 4MS3 indicated a binding affinity of -3.2 kcal.mol⁻¹, due to a very close H-bond interaction which is close and strong enough to be considered a covalent interaction at a distance of 1.89Å between the N-atom of (1) and the SER-A:131 residue. Also, a pi-alkyl hydrophobic interaction was observed between the pi-electrons in the aromatic (benzene) ring system of (1) and PRO-A:105 residue at an extracellular distance of 5.26 Å. The interaction between DZP and 4MS3 receptor protein indicated a binding affinity of 12.6 kcal.mol⁻¹, which is poor and attributed to more unfavourable bump-repulsive ionic interactions compared to the weak favourable hydrophobic ones, between the DZP and 4MS3 receptor. The interaction indicated unfavourable bump at a distance of 2.18, 2.23, 2.16, 2.45, 2.32 and 2.46 Å between THR-A:199 and the aromatic ring of DZP and 2.03Å. The favourable interactions were Pi-Sulphur with sulphur in CYS-A:103 and the pi-electrons in the DZP ring system at distance of 5.52Å and Alkyl and pi-alkyl interactions with VAL-A:201. This unfavourable bump, greatly reduced the binding affinity. Figure 17 (b) showed that DZP is not located in the Venus flytrap extracellular module, so it's not a potential agonist for GABA_B receptor the management of spasmodic activity associated with CNS disorder. The interaction between the studied compound (1) and 4MS3 occupied the Venus flytrap extracellular cavity of the GABA_B receptor just as described by Zhu, *et al.*, and therefore, may share similar mechanism with benzodiazepines [50]. Therefore, this study provides a template for understanding the bioactivity of (1) and will assist rational approaches to its therapeutic application as a muscle relaxant (antispasmodic) and associated neurological disorders and mental illness by targeting GABA_B receptor protein.

Conclusion

In this study, the synthesis, crystallography and theoretical structural, electronic, topological and vibrational investigation of a novel perchlorate organic-inorganic hybrid material is reported. The theoretical investigations were accomplished on the framework of density functional theory (DFT) by deploying the highly parameterized functional of the Minnesota class (M06-2X) and the PWPB95 D3BJ functional for benchmarking purposes. In all cases, the split valence basis set (6-311 ++ G(2df, 2pd) with large polarization function, the Duning basis set (aug-cc-pVTZ), and the def2-TZVP basis set was utilized. Molecular electronic properties such as the frontier molecular orbitals, natural bond orbital analysis, molecular electrostatic potential, Hirshfeld surface analysis and vibrational specificities including *in-silico* bioactivity prediction of the studied hybrid material were considered to espy the various molecular attribute which could prime the effective utilization of the synthesized cluster for various pharmacological applications. The results generally disclose interesting properties for the hybrid material, the geometrical attributes in relation with the crystallographic data are perfectly harmonized. The root mean square deviation of the computed geometric properties form the experimental data is within 0.058 and 0.89 Å which indicates good conformity. The molecular electronic properties in terms of the energy gap and IP as hypothesized by Koopman divulged the compound to be considerably stable and possess high propensity for electron acceptance and a considerable aptitude to exchange electron density with external electronic environment. Due to the paramagnetic nature of spin density, electronic distribution is condensed over the cation and anion moiety of the perchlorate cluster and as such

explicates different potential sites for both electrophilic and nucleophilic substitution as evident in the molecular electrostatic potential isosurface and Mullikan charge distribution. Also, the calculations demonstrate that antispasmodic potency as exhibited by the studied compound is strongly dependent on its structural diversity and spin density localization, the high concentration of charge density around the chlorate ion and aromatic ring facilitates the effective binding interactions with GABA receptor in a mechanism that is quite similar to already established spasmodic modulators. The findings therefore contribute to the wholistic comprehension of the pharmacological potential and molecular attributes of the studied compound from the molecular and structural perspective and could therefore, be exploited in pharmacology or electronic material hybrid technology.

Declarations

Funding: Not funded

Conflict of interest: Authors declare zero conflict of interest

Availability of data and material: All data are available within the manuscript and associated supporting information file

Code availability: Not applicable

Authors' contributions: Emna Jaziri: data curation. Hitler Louis: Computational resources writing and proofreading. Chaima Gharbi: Hirshfeld surface and contact enrichment study. Tomsmith O. Unimuke: Computational investigation. Ernest C. Agwamba: In-silico investigation and writing. Gideon E. Mathias: Formal analysis. Wataru Fugita: X-ray data collections and structure resolution. Chérif Ben Nasr and Lamia Khedhiri: Conceptualization, writing, editing and supervision

Acknowledgment

The center for high performance computing, Johannesburg, South Africa is acknowledged for providing computational resources for this study.

References

1. T. Trindade, P. O'Brien, N. L. Pickett, Nanocrystalline Semiconductors: Synthesis, Properties, and Perspectives, *Chem. Mater.* 13 (2001) 3843-3858. <https://doi.org/10.1021/cm000843p>
2. A. N. Shipway, E. Katz, I. Willner, Nanoparticle arrays on surfaces for electronic, optical, and sensor applications, *Chemphyschem* 1 (2000) 18-52. DOI: 10.1002/1439-7641(20000804)1:1<18::AID-CPHC18>3.0.CO;2-L
3. M. C. Daniel, D. Astruc, Gold Nanoparticles: Assembly, Supramolecular Chemistry, Quantum-Size-Related Properties, and Applications toward Biology, Catalysis, and Nanotechnology, *Chem. Rev.* 104 (2004) 293-346. <https://doi.org/10.1021/cr030698+>
4. A. K. Vishwakarma, P. S. Ghalsasi, A. Navamoney, Y. Lan, A. K. Powell, Structural phase transition and magnetic properties of layered organic-inorganic hybrid compounds: *p*-Haloanilinium tetrachlorocuparate(II), *Polyhedron.* 30 (2011) 1565- 1570. <https://doi.org/10.1016/j.poly.2011.03.025>
5. T. L. Fonseca, H. C. B. de Oliveira, O. A. V. Amaral, M. A. Castro, MP2 static first hyperpolarizability of azo-enaminone isomers, *Chem. Phys. Lett.* 413 (2005) 356-361. <https://doi.org/10.1016/j.cplett.2005.08.007>
6. H. B. Duan, S. S. Yu, H. Zhou, Alternating-current conductivity and dielectric relaxation of bulk iodoargentate, *Mater. Res. Bull.* 65 (2015) 137-141. <https://doi.org/10.1016/j.materresbull.2015.01.049>.
7. P. Szklarz, R. Jakubas, G. Bator, T. Lis, V. Kinzhybalov, J. Baran, Structural characterization, spectroscopic properties and phase transition in 4-aminopyridinium tetrachlorogallate(III): [4-NH₂PyH][GaCl₄], *J. Phys. Chem. Solids.* 68 (2007) 2303- 2316. <https://doi.org/10.1016/j.jpcs.2007.06.022>

8. M. Ben Gzaiel, A. Oueslati, M. Gargouri, Ac Conductivity and Transport Properties of $[N(C_3H_7)_4]_2Zn_2Cl_6$ Compound, *J. Clust. Sci.* 26 (2015) 1577–1594. <https://doi.org/10.1007/s10876-015-0852-3>
9. I. Bayar, L. Khedhiri, E. Jeanneau, F. Lefebvre, C. Ben Nasr, Synthesis, structural study and characterization of two new $(ClC_7H_6NH_3)ClO_4 \cdot H_2O$ isostructural hydrates of isomeric organic amine perchlorates. *J. Mol. Struct.* 1211 (2020) 128078. <https://doi.org/10.1016/j.molstruc.2020.128078>
10. I. Bayar, L. Khedhiri, E. Jeanneau, F. Lefebvre, C. Ben Nasr, Crystal structure, quantum mechanical study and spectroscopic studies of nitrate and perchlorate salts of 3-chloroaniline, $[C_6H_7ClN]NO_3$ (I) and $[C_6H_7ClN]ClO_4$ (II). *J. Mol. Struct.* 1137 (2017) 373-379. <https://doi.org/10.1016/j.molstruc.2017.02.042>
11. C. Peltinari, F. Marchetti, M. Pelli, A. Cingolani, L. Barba, A. Cassetta, Tin(IV) and organotin(IV) complexes containing mono or bidentate N-donor ligands II. ¹4-Phenylimidazole derivatives. Crystal and molecular structure of [bis(4-phenylimidazole) trimethyltin(IV)] chloride, *J. Organomet. Chem.* 515 (1996) 119- 130. [https://doi.org/10.1016/0022-328X\(95\)06054-Z](https://doi.org/10.1016/0022-328X(95)06054-Z)
12. S. K. Vasisht, T. P. Kaur, J. Kaushal, S. Dixit, Synthesis and characterization of sodium bis(trimethylstannyl) amide and bis(trimethylsilyl) bis(trimethylstannyl) - phospho-tetrazene, *J. Organomet. Chem.* 540 (1997) 51-54. [https://doi.org/10.1016/S0022-328X\(97\)00093-4](https://doi.org/10.1016/S0022-328X(97)00093-4)
13. M. Gielen, Tin-based antitumour drugs, *Coord. Chem. Rev.* 151 (1996) 41-51. [https://doi.org/10.1016/S0010-8545\(96\)90193-9](https://doi.org/10.1016/S0010-8545(96)90193-9).
14. K. Kaabi, M. El Glaoui, V. Ferretti, M. Zeller, C. Ben Nasr, 2-Amino-4-methyl-6-oxo- 3,6-dihydropyrimidin-1-ium perchlorate-2-amino-6-methylpyrimidin-4(1*H*)-one-water (1/1/1). *Acta Cryst E67* (2011). o2507-o2508. <https://doi.org/10.1107/S1600536811034106>
15. L. Bendjeddou, A. Cherouana, N. Hadjadj, S. Dahaouib, C. Lecomteb, Adeninium 3- carboxyanilinium bis(perchlorate) trihydrate, *Acta Cryst. E65* (2009) o2303-o2304. <https://doi.org/10.1107/S1600536809034199>
16. C. Peng, *Acta Cryst E66* (2010) 2214.
17. H. M. Ahmed, Investigation of Rosemary Herbal Extracts (*Rosmarinus Officinalis*) and Their Potential Effects on Immunity. (2020), No. January, 1–9. <https://doi.org/10.1002/ptr.6648>.
18. Y. Geng, M. Bush, L. Mosyak, F. Wang, Q. R. Fan, Structural Mechanism of Ligand Activation in Human GABA B Receptor. *Nature* 35 (2013) 1–8. <https://doi.org/10.1038/nature12725>.
19. K. Wei, H. Louis, W. Emori, P. S. Idante, E. C. Agwamba, C.-R. Cheng, E. A. Eno T. O. Unimuke, Antispasmodic Activity of Carnosic Acid Extracted from *Rosmarinus Officinalis*: Isolation, Spectroscopic Characterization, DFT Studies, and in Silico Molecular Docking Investigations. *J. Mol. Struct.*, (2022), 132795. <https://doi.org/10.1016/j.molstruc.2022.132795>.
20. G. E. Lind, T. Mou, L. Tamborini, M. G. Pomper, C. De Micheli, P. Conti, Structural Basis of Subunit Selectivity for Competitive NMDA Receptor Antagonists with Preference for GluN2A over GluN2B Subunits. *Proc Natl Acad Sci U S A*, 114 (2017) E6942-E6951. <https://doi.org/10.1073/pnas.1707752114>.
21. J. Changeux, S. J. Edelman, The nicotinic acetylcholine receptor: From molecular biology to cognition. *Neuropharmacology* 96 2005. <https://doi.org/10.1016/j.neuropharm.2015.03.024>.
22. R. C. Hogg, M. Raggenbass, D. Bertrand, Nicotinic Acetylcholine Receptors: From Structure to Brain Function. *Rev. Physiol. Biochem. Pharmacol.* 147 (2003) 1–46. <https://doi.org/10.1007/s10254-003-0005-1>.
23. I. Benjamin, A. D. Udoikono, H. Louis, E. C. Agwamba, T. O. Unimuke, A. E. Owen A. S. Adeyinka, Antimalarial Potential of Naphthalene-Sulfonic Acid Derivatives: Molecular Electronic Properties, Vibrational Assignments, and in-Silico Molecular Docking Studies. *J. Mol. Struct.*, 1264 (2022) 133298. <https://doi.org/https://doi.org/10.1016/j.molstruc.2022.133298>.
24. E. C. Agwamba, A. D. Udoikono, H. Louis, E. U. Udoh, I. Benjamin, A. T. Igbalagh; H. O. Edet, E. U. Ejiofor, U. B. Ushaka, Synthesis, Characterization, DFT Studies, and Molecular Modeling of Azo Dye Derivatives as Potential Candidate for

- Trypanosomiasis Treatment. Chem. Phys. Impact 4 (2022) 100076. <https://doi.org/10.1016/j.chphi.2022.100076>.
25. F. S. Patrick-Inezi, W. Emori, H. Louis, C. G. Apebende, E. C. Agwamba, T. O. Unimuke, K. Wei, C.-R. Cheng, V. M. Bassey, T. C. Egemonye, Analeptic Activity of 2-Hydroxyl-5-Nitrobenzaldehyde: Experimental, DFT Studies, and in Silico Molecular Docking Approach. Healthc. Anal. 2 (2022) 100030. <https://doi.org/10.1016/j.health.2022.100030>.
 26. W. Emori, G. J. Ogunwale, H. Louis, E. C. Agwamba, K. Wei, T. O. Unimuke, C.-R. Cheng, E. U. Ejiofor, F. C. Asogwa, A. S. Adeyinka, Spectroscopic (UV-Vis, FT-IR, FT-Raman, and NMR) Analysis, Structural Benchmarking, Molecular Properties, and the in-Silico Cerebral Anti-Ischemic Activity of 2-Amino-6-Ethoxybenzothiazole. J. Mol. Struct. 1265 (2022) 133318. <https://doi.org/https://doi.org/10.1016/j.molstruc.2022.133318>.
 27. A. D. Udoikono, H. Louis, E. A. Eno, E. C. Agwamba, T. O. Unimuke, A. T. Igbalagh, H. O. Edet, J. O. Odey, A. S. Adeyinka, Reactive Azo Compounds as a Potential Chemotherapy Drugs in the Treatment of Malignant Glioblastoma (GBM): Experimental and Theoretical Studies. J. Photochem. Photobiol., 10 (2022), 100116. <https://doi.org/10.1016/j.jpap.2022.100116>.
 28. U. J. Undiandeye, H. Louis, T. E. Gber, T. C. Egemonye, E. C. Agwamba, I. A. Undiandeye, A. S. Adeyinka, B. I. Ita, Spectroscopic, Conformational Analysis, Structural Benchmarking, Excited State Dynamics, and the Photovoltaic Properties of Enalapril and Lisinopril. J. Indian Chem. Soc. 99 (2022) 100500. <https://doi.org/https://doi.org/10.1016/j.jics.2022.100500>.
 29. T. Hiteshi, C. Tanmoy, S. Vandana, A brief review on importance of DFT in drug design. Res Med Eng Sci. 7 (2019) 791-795. <http://dx.doi.org/10.31031/RMES.2019.07.000668>
 30. V. T. Sabe, T. Ntombela, L. A. Jhamba, G. E. M. Maguire, T. Govender, T. Naicker, H. G. Kruger, Current trends in computer aided drug design and a highlight of drugs discovered via computational techniques: A review, Eur. J. Med. Chem. 224 (2021) 113705. <https://doi.org/10.1016/j.ejmech.2021.113705>
 31. T. O. Unimuke, H. Louis, E. A. Eno, E. C. Agwamba, A. S. Adeyinka, Meta-Hybrid Density Functional Theory Prediction of the Reactivity, Stability and IGM of Azepane, Oxepane, Thiepane and Halogenated Cycloheptane. ACS Omega, 7 (2022) 13704-13720. <https://doi.org/10.1021/acsomega.1c07361>.
 32. G. M. Sheldrick, A Short History of SHELX, Acta Crystallographica A64 (2008) 112- 122. <http://dx.doi.org/10.1107/S0108767307043930>
 33. G. M. Sheldrick, Crystal Structure Refinement with SHELXL, Acta Crystallographica C71 (2015), 3-8. <http://dx.doi.org/10.1107/S2053229614024218>
 34. L. J. Farrugia, WinGX Suite for Small-Molecule Single-Crystal Crystallography, J. Appl. Crystallography, 32 (1999) 837-838. doi:10.1107/S0021889899006020
 35. K. Brandenburg, Diamond Version 2.0 Impact GbR. Bonn, Germany (1998).
 36. M. J. Turner, S. Grabowsky, D. Jayatilaka, M. A. Spackman, Accurate and efficient model energies for exploring intermolecular interactions in molecular crystals. J. Phys. Chem. Lett. 5 (2014) 4249-4255. <https://doi.org/10.1021/jz502271c>
 37. M. J. Frisch, G. W. Trucks, H. B. Schlegel, G. E. Scuseria, M. A. Robb, J. R. Cheeseman, G. Scalmani, V. Barone, B. Mennucci, G. A. Petersson, H. Nakatsuji, M. Caricato, X. Li, H. P. Hratchian, A. F. Izmaylov, J. Bloino, G. Zheng, J. L. Sonnenberg, M. Hada, M. Ehara, K. Toyota, R. Fukuda, J. Hasegawa, M. Ishida, T. Nakajima, Y. Honda, O. Kitao, H. Nakai, T. Vreven, J. A. Montgomery, Jr., J. E. Peralta, F. Ogliaro, M. Bearpark, J. J. Heyd, E. Brothers, K. N. Kudin, V. N. Staroverov, R. Kobayashi, J. Normand, K. Raghavachari, A. Rendell, J. C. Burant, S. S. Iyengar, J. Tomasi, M. Cossi, N. Rega, J. M. Millam, M. Klene, J. E. Knox, J. B. Cross, V. Bakken, C. Adamo, J. Jaramillo, R. Gomperts, R. E. Stratmann, O. Yazyev, A. J. Austin, R. Cammi, C. Pomelli, J. W. Ochterski, R. L. Martin, K. Morokuma, V. G. Zakrzewski, G. A. Voth, P. Salvador, J. J. Dannenberg, S. Dapprich, A. D. Daniels, Ö. Farkas, J. B. Foresman, J. V. Ortiz, J. Cioslowski, and D. J. Fox, *Gaussian 09* (Gaussian, Inc., Wallingford CT, 2016).

38. E. D. Glendening, R. L. Clark, F. Weinhold, NBO 7.0: New vistas in localized and delocalized chemical bonding theor, *J. comput. chem.* 40 (2019): 2234-2241. <https://doi.org/10.1002/jcc.25873>
39. T. Lu, F. Chen. Multiwfn: a multifunctional wavefunction analyzer. *J. Comput. Chem.* 33 (2012) 580-592. <https://doi.org/10.1002/jcc.22885>
40. The Pymol Molecular graphics system, version 1.2r3pre, Schrodinger LLC.
41. Biova, Dassault System, [Software Product name 1], [Software version 1]; [Software product name 2], San Diego : Dassult Systemes, [2021].
42. O. Trott, A. J. Olson, AutoDock Vina: improving the speed and accuracy of docking with a new scoring function, efficient optimization and multithreading, *J. Comput. Chem.* 31 (2010) 455-461 <https://doi.org/10.1002/jcc.21334>
43. [43] L. Jendele, R. Krivak, P. Skoda, M. Novotny, D. Hoksza, PrankWeb: a web server for ligand binding site prediction and visualization, *Nucleic Acids Res.* 47 (2019) W345-W349. <https://doi.org/10.1093/nar/gkz424>.
44. T. O. Unimuke, H. Louis, W. Emori, P. S. Idante, E. C. Agwamba, I. C. Nwobodo, K. Wei, C.-R. Cheng, S. A. Adalikwu, V. M. Bassey. Spectroscopic and Molecular Electronic Property Investigation of 2-Phenylpyrimidine-4, 6-Diamine via ¹H-NMR, UV-Vis, FT-Raman, FT-IR, and DFT Approach. *J. Mol. Struct.* 1263 (2022), 133195. <https://doi.org/https://doi.org/10.1016/j.molstruc.2022.133195>.
45. M. Khalid, R. Jawaria, M. U. Khan, A. A. C. Braga, Z. Shafiq, M. Imran, H. M. A. Zafar A. Irfan, An efficient synthesis, spectroscopic characterization, and optical nonlinearity response of novel salicylaldehyde thiosemicarbazone derivatives. *ACS omega* 6 (2021) 16058-16065. <https://doi.org/10.1021/acsomega.1c01938>
46. T. Koopmans. On the assignment of wave functions and eigenvalues to the individual electrons of an atom. *Physica* 1 (1934) 104-115.
47. M. D. Mohammadi, H. Y. Abdullah, H. Louis, E. M. Gideon, 2D Boron Nitride Material as a sensor for H₂SiCl₂. *J. Theor. Comput. Chem.* 1213 (2022) 113742. <https://doi.org/10.1016/j.comptc.2022.113742>
48. M. C. F. Bautista, D. Cortes-Arriagada, E. Shakerzadeh, E. C. Anota, Acetylsalicyclid acid interaction with Boron nitride nanostructures-A density functional analysis. *J. Mol. Liq.* 355 (2022) 118980. <https://doi.org/10.1016/j.molliq.2022.118980>
49. E. A. Eno, H. Louis, T. O. Unimuke, T. E. Gber, I. J. Mbonu, C. J. Nkubisi, S. A. Adalikwu, Reactivity, Stability, and thermodynamics of Para-methylpyridinium-based ionic liquids: insight from DFT, NCI, and QTAIM. *J. ionic Liquids* 2 (2022), 100030. <https://doi.org/10.1016/j.jil.2022.100030>
50. S. Zhu, C. M. Noviello, J. Teng, R. M. W. Jr, J. J. Kim, R. E. Hibbs, Structure of a human synaptic GABA_A receptor. *Nature* 559 (2018) 67–72. <https://doi.org/10.1038/s41586-018-0255-3>.

Figures

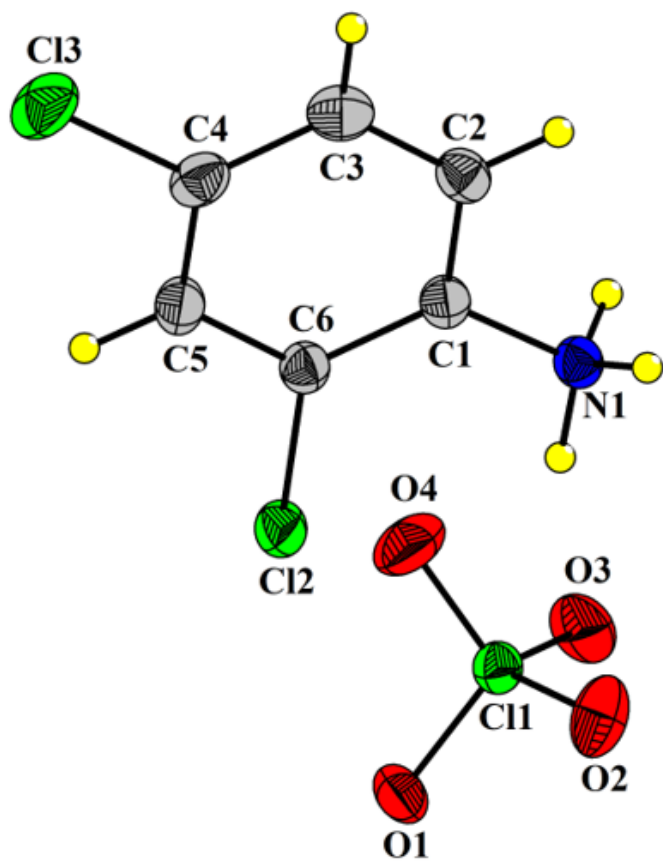


Figure 1

Molecular structure of [C₆H₆Cl₂N]ClO₄ with the numbering scheme for the atoms and 50% probability displacement ellipsoids.

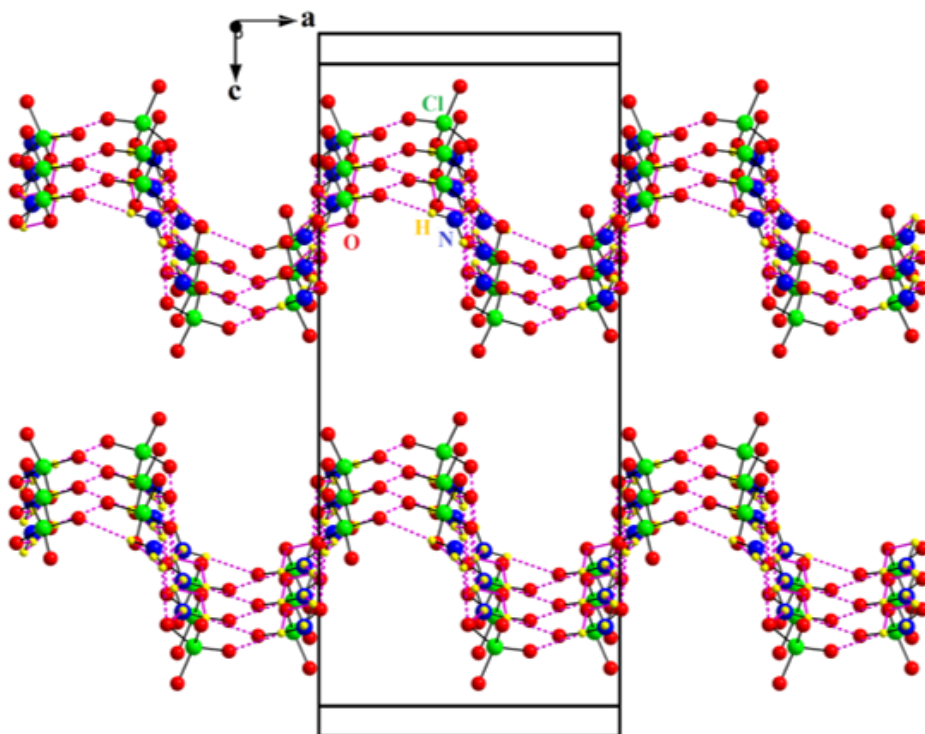


Figure 2

Corrugated inorganic layers in $[\text{C}_6\text{H}_6\text{Cl}_2\text{N}]\text{ClO}_4$. Hydrogen bonds are shown as dashed lines

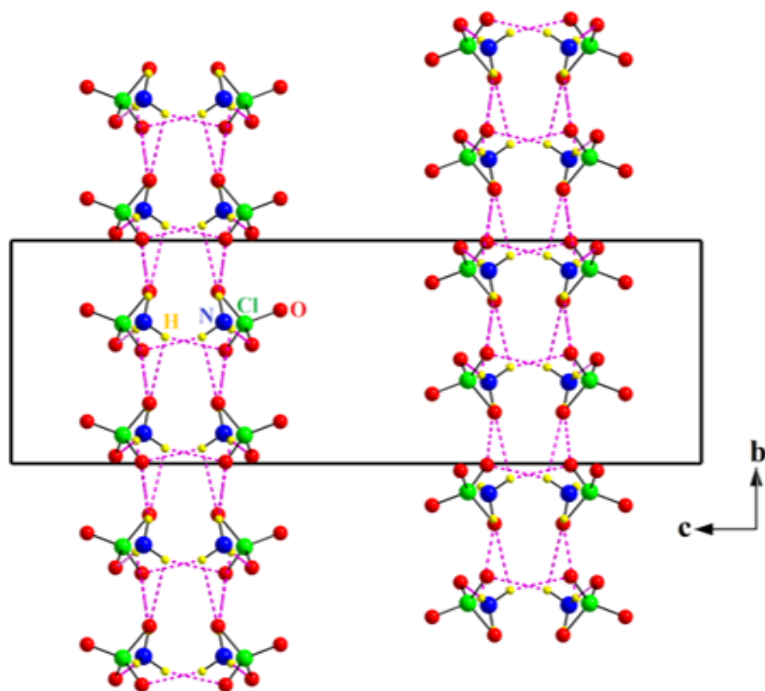


Figure 3

Inorganic layers in $[\text{C}_6\text{H}_6\text{Cl}_2\text{N}]\text{ClO}_4$ developed along b -axis direction at $z=1/4$ and $z=3/4$. Hydrogen bonds are drawn as dashed lines.

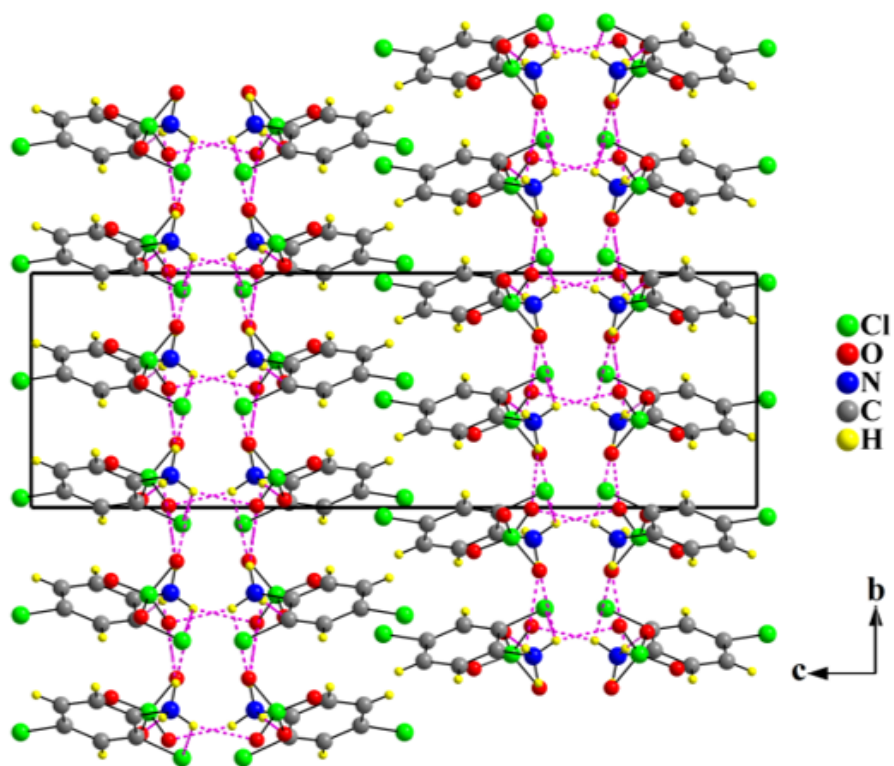


Figure 4

A packing diagram of $[\text{C}_6\text{H}_6\text{Cl}_2\text{N}]\text{ClO}_4$, viewed down the a -axis. Hydrogen bonds are drawn as dashed lines.

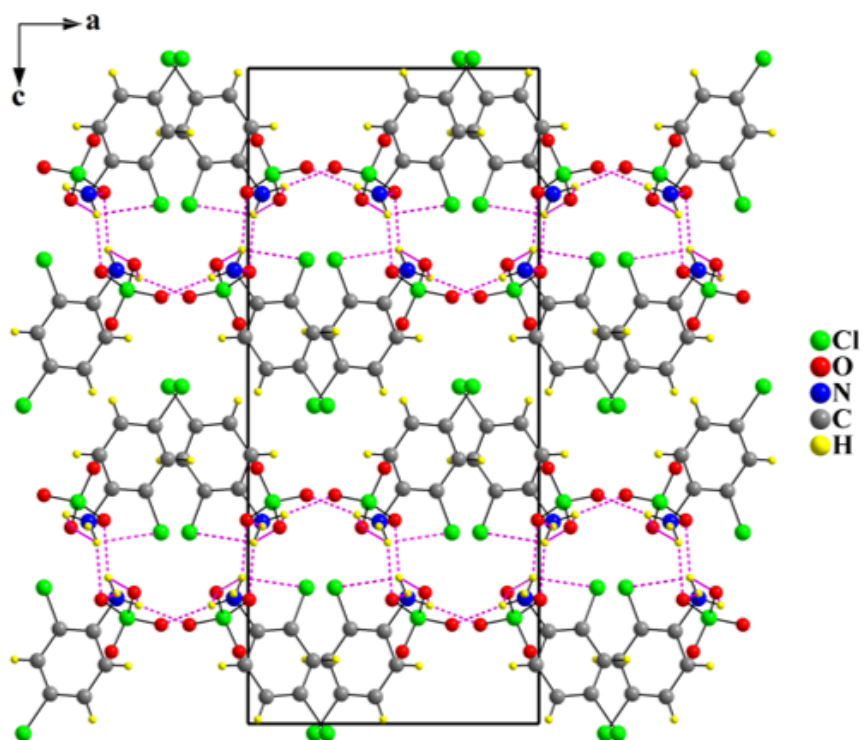


Figure 5

A packing diagram of $[\text{C}_6\text{H}_6\text{Cl}_2\text{N}]\text{ClO}_4$, viewed down the b -axis. Hydrogen bonds are drawn as dashed lines.

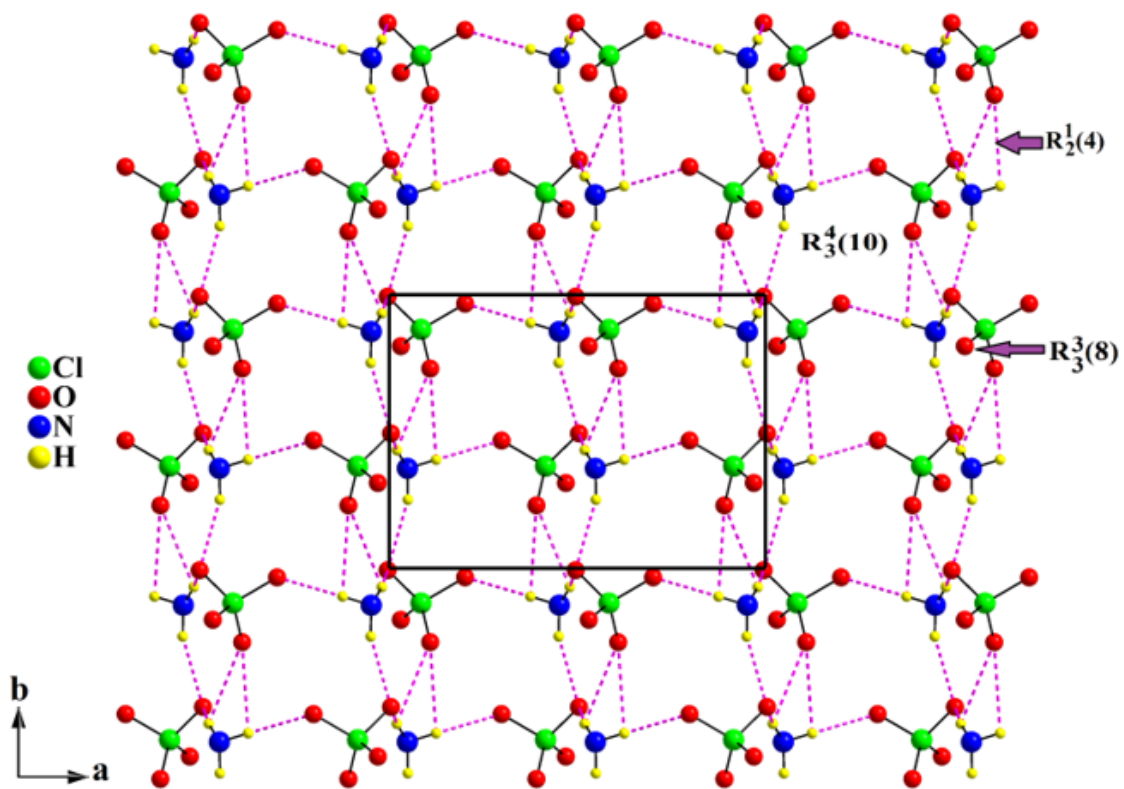


Figure 6

Projection of one inorganic layer at $z=1/4$ showing graph-set motifs in $[\text{C}_6\text{H}_6\text{Cl}_2\text{N}] \text{ClO}_4$

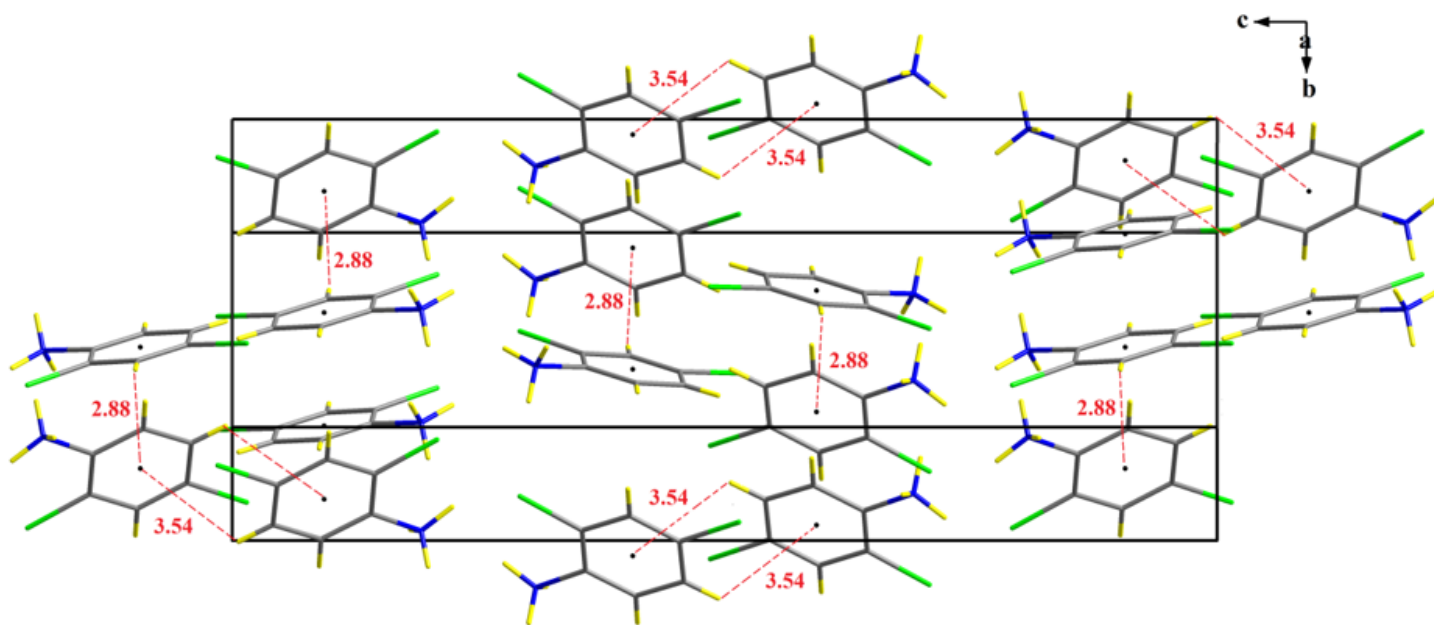


Figure 7

A perspective view of the organic packing in $[\text{C}_6\text{H}_6\text{Cl}_2\text{N}]\text{ClO}_4$. Dashed lines indicate hydrogen C-H...p interactions.

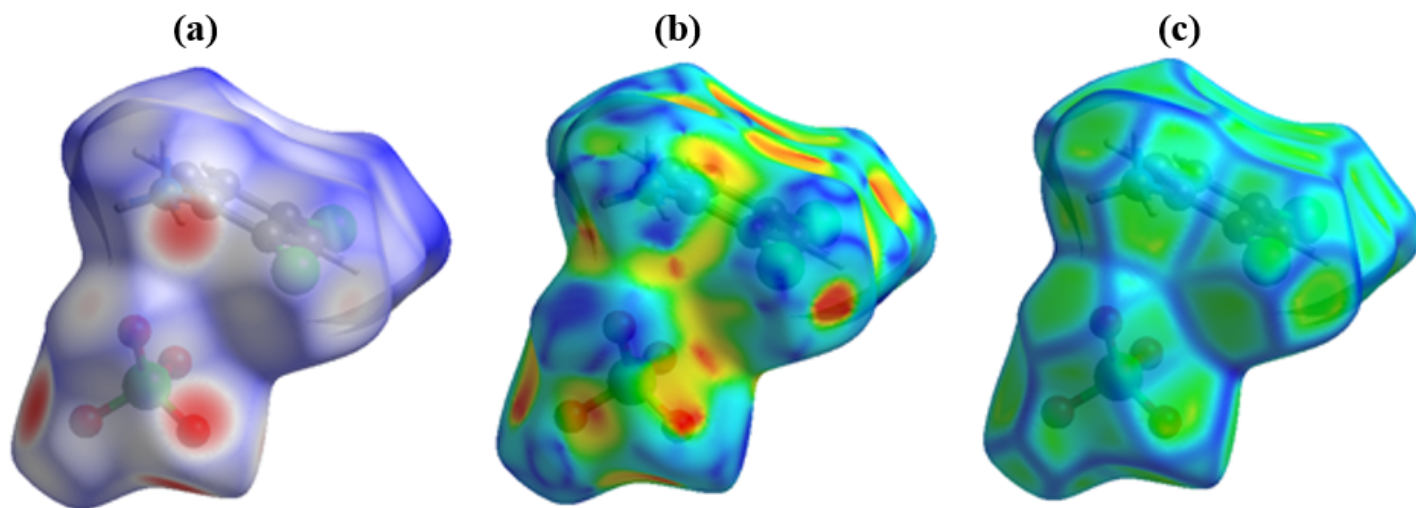


Figure 8

Hirshfeld surfaces mapped with d_{norm} (a), shape index (b) and curvedness (c) for $[\text{C}_6\text{H}_6\text{Cl}_2\text{N}]\text{ClO}_4$.

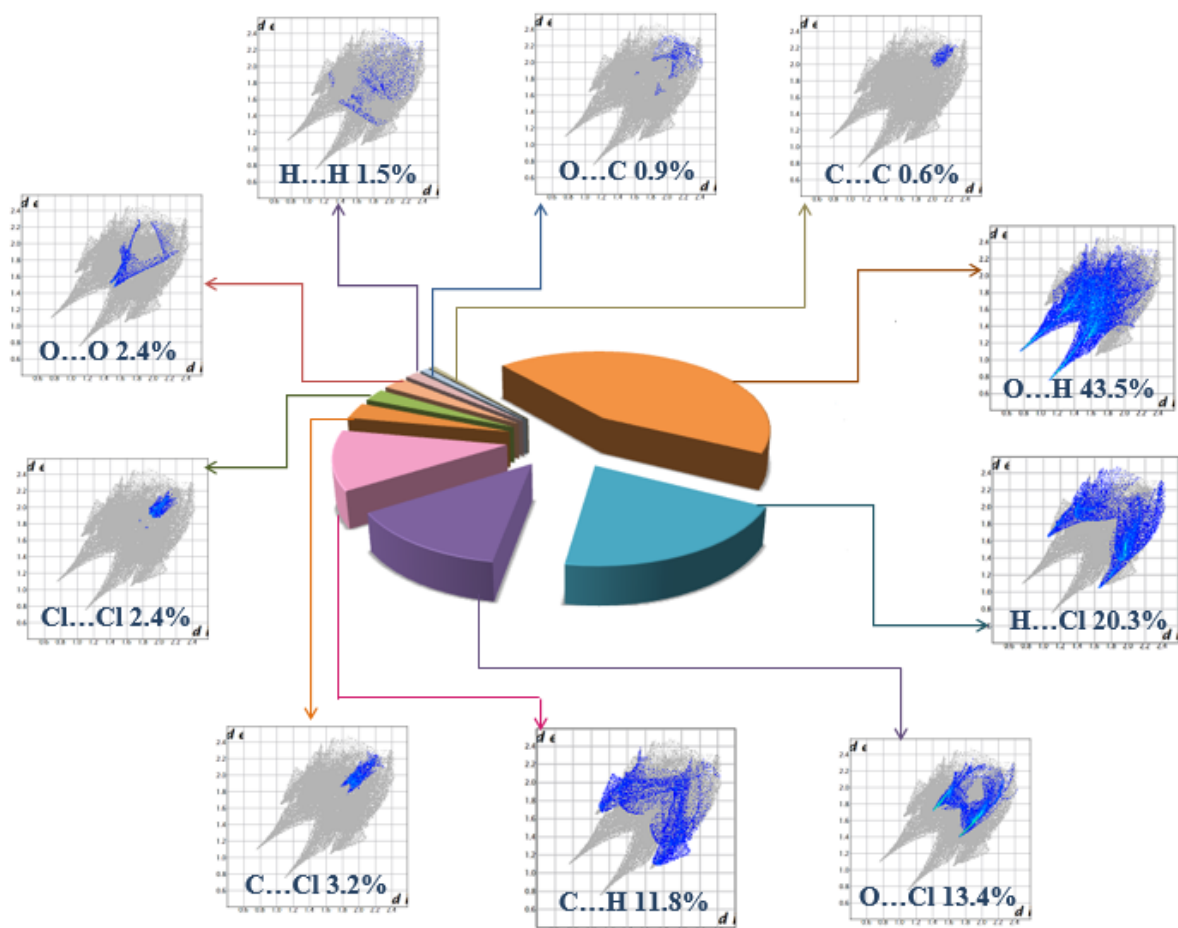


Figure 9

The relative contributions and 2D Fingerprint plots of different intermolecular interactions to the Hirshfeld surface area for $(C_6H_6Cl_2N)ClO_4$.

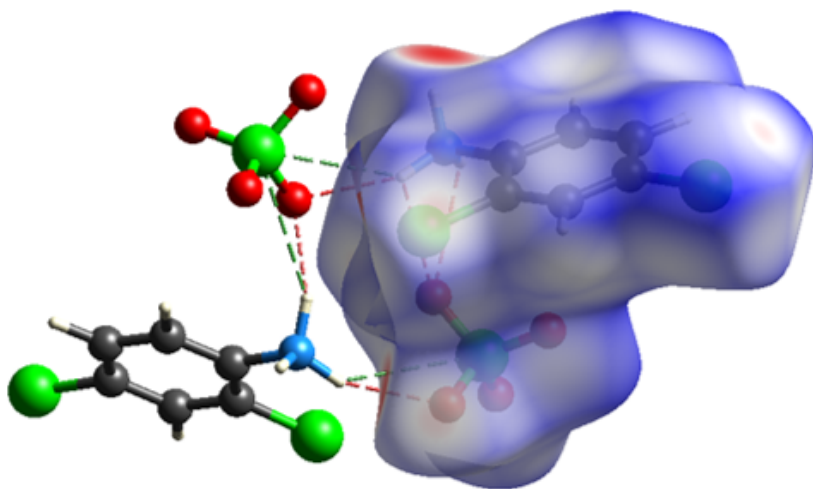


Figure 10

Hirshfeld surfaces mapped with d_{norm} of the asymmetric unit of the title compound. Intermolecular contacts are shown in dotted lines.

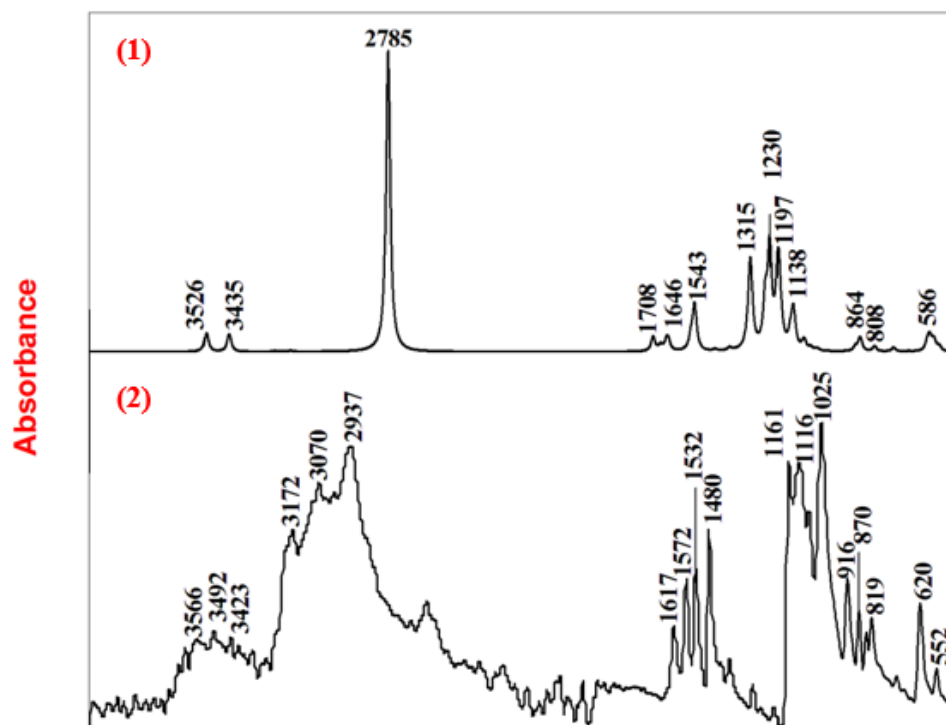


Figure 11

Superposition of theoretical (1) and experimental (2) infrared absorption spectra of $(\text{C}_6\text{H}_6\text{Cl}_2\text{N})\text{ClO}_4$.

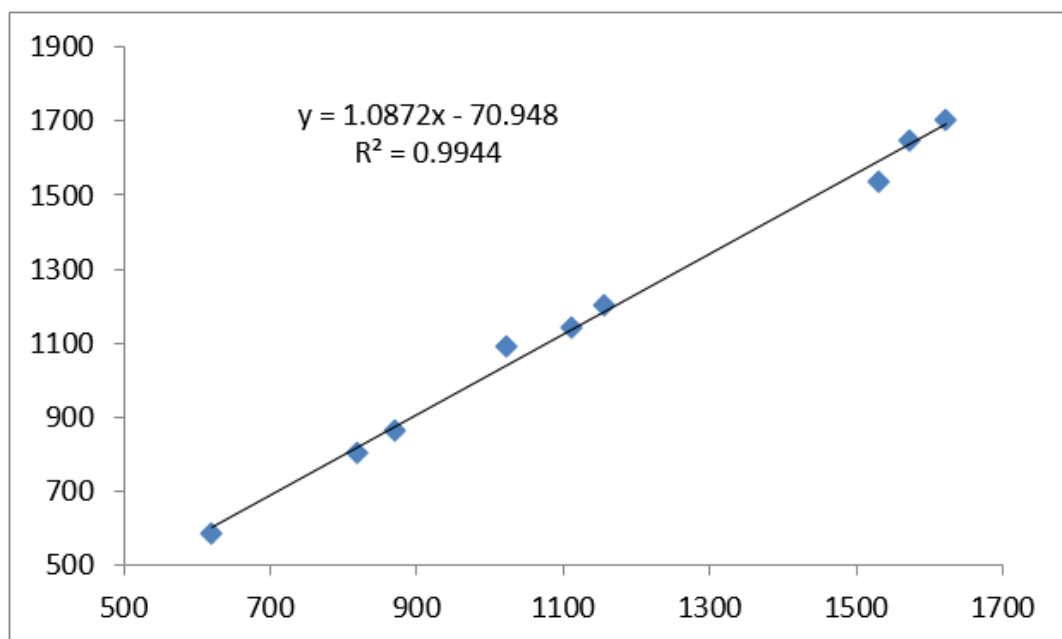


Figure 12

Comparison between experimental and calculated IR frequencies.

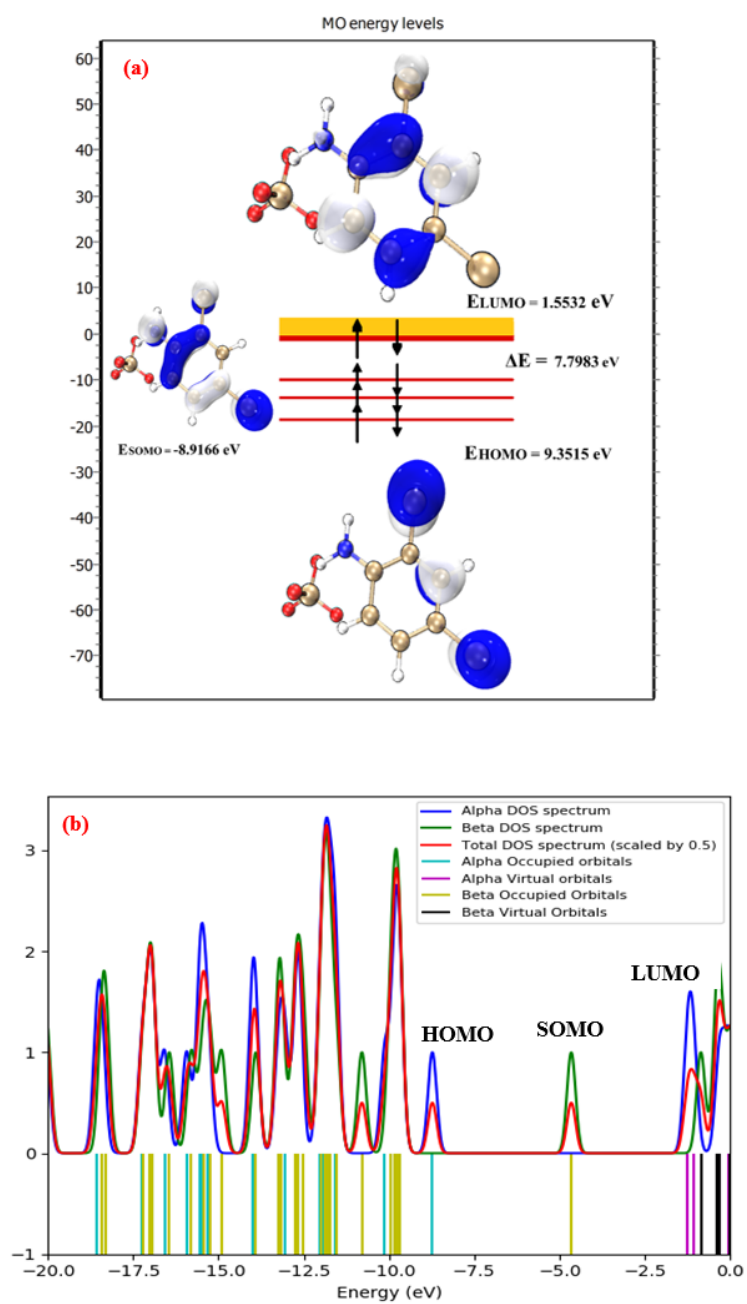


Figure 13

(a) Frontier orbitals of the studied compound and (b) energy distribution of the different orbitals of (I)

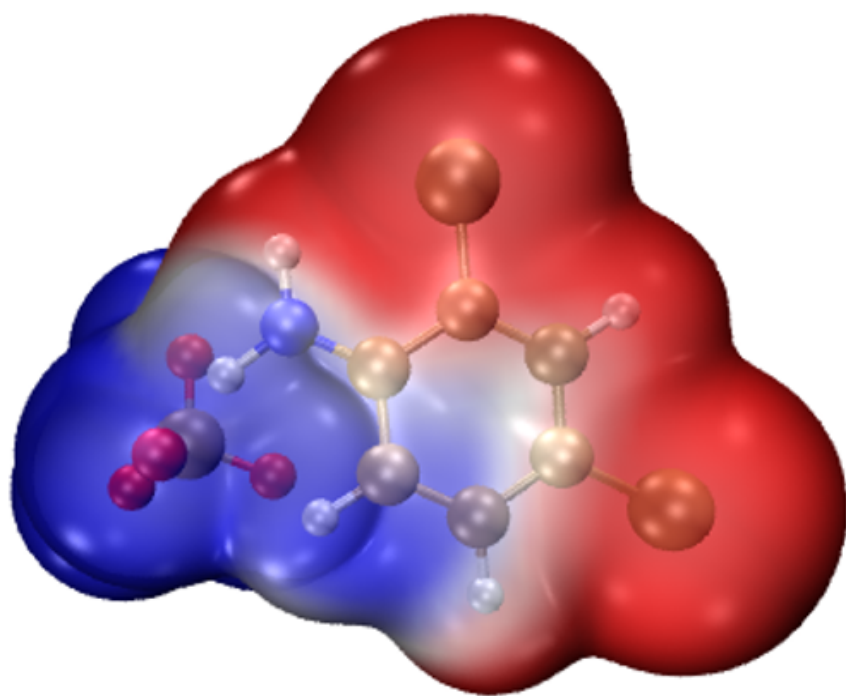


Figure 14

MEP surfaces of $(C_6H_6Cl_2N)ClO_4$

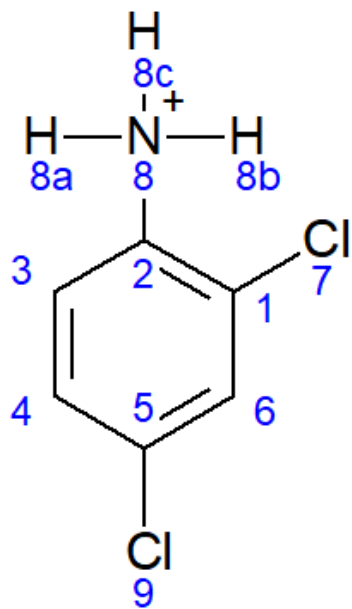


Figure 15

Numbering atoms of the organic molecule in (I)

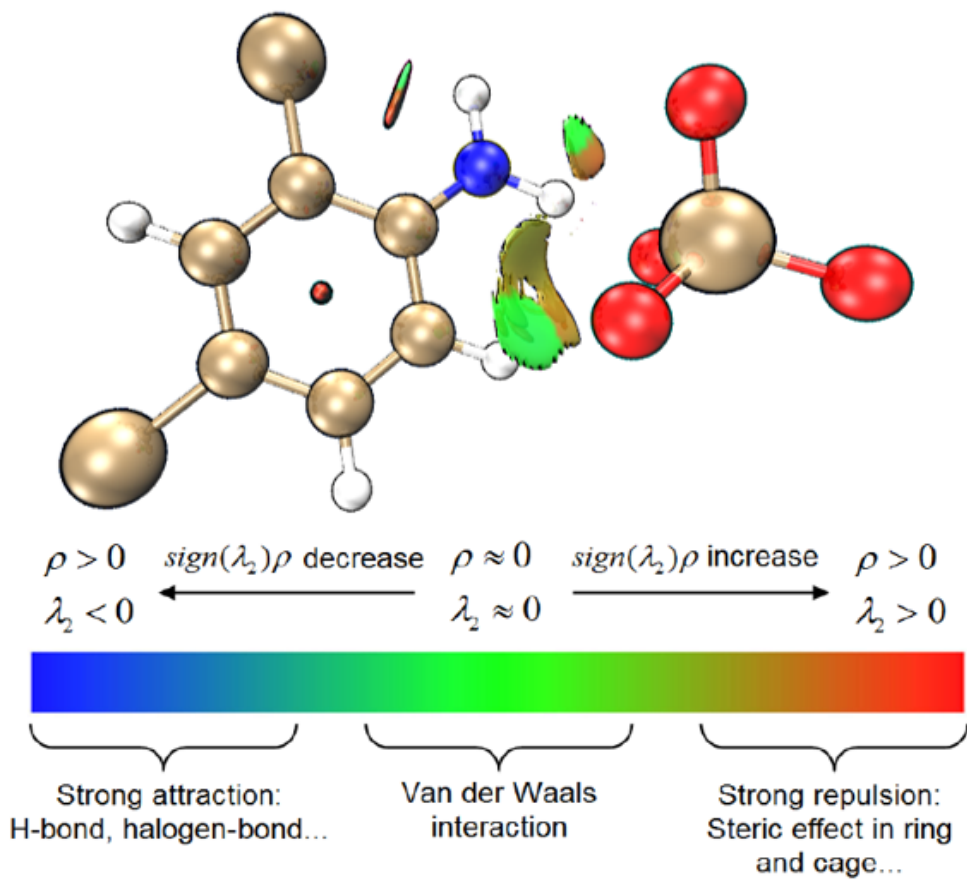
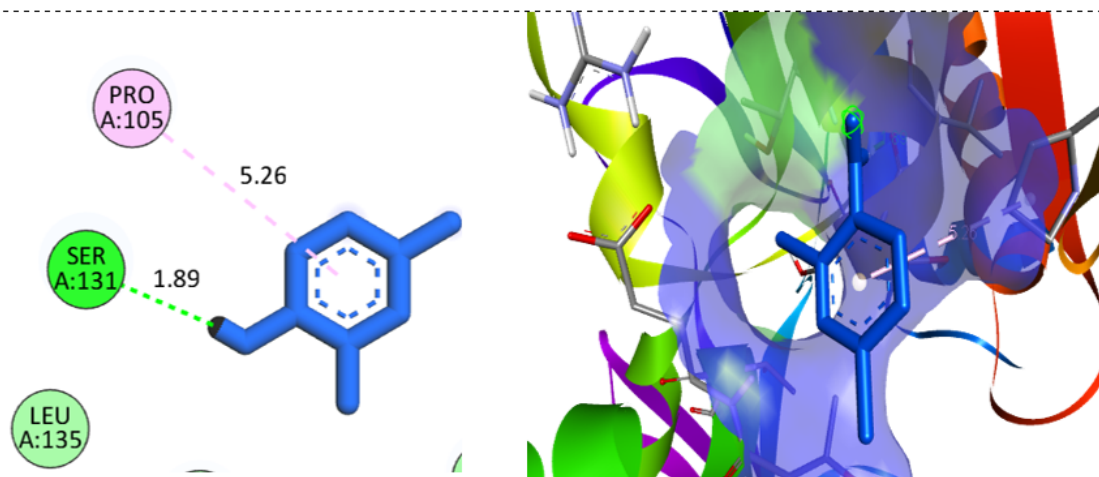


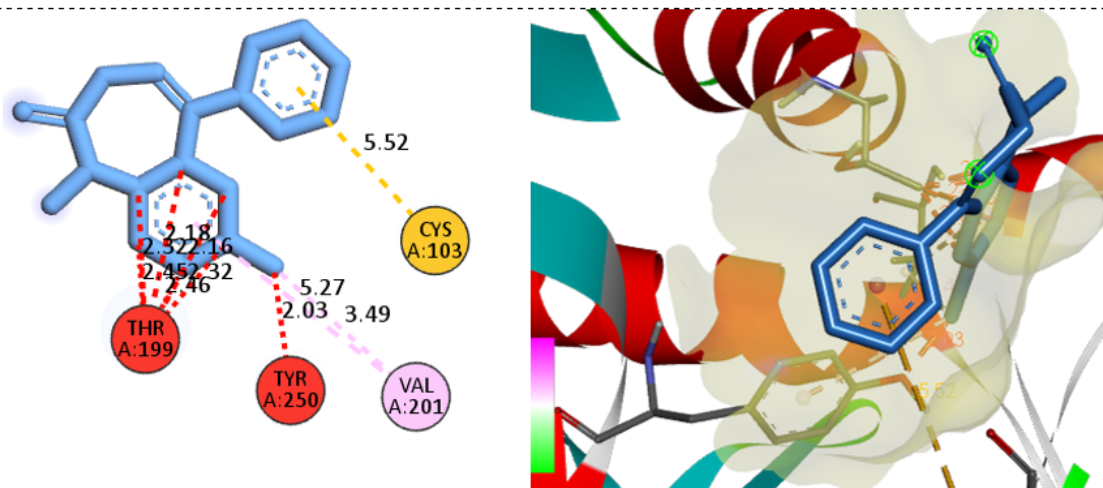
Figure 16

visualization of non-covalent interaction between the anion and cation fragments



Binding Affinity = $-3.2 \text{ kcal.mol}^{-1}$

(a) (1)-4MS3 complex



Binding Energy = $12.6 \text{ kcal.mol}^{-1}$

(b). DZP-4MS3 complex

Figure 17

2D and 3D representation of Ligand and amino acid interactions of (a) studied compound (1) and (b) benzodiazepam (DZP) with Human GABAB (c-aminobutyric acid class B) receptor protein (4MS3)

Supplementary Files

This is a list of supplementary files associated with this preprint. Click to download.

- [Supportinginformationfile.docx](#)